Bull. Chem. Soc. Jpn., 73, 1445—1460 (2000) 1445

Accounts

Gold Valence Transition and Phase Diagram in the Mixed-Valence Complexes, $M_2[Au^IX_2][Au^{III}X_4]$ (M = Rb, Cs; X = Cl, Br, and I)

Norimichi Kojima

Department of Basic Science, Graduate School of Arts and Sciences, The University of Tokyo,
Komaba 3-8-1, Meguro-ku, Tokyo 153-8902

(Received December 20, 1999)

In this paper, I review the structural and physical properties of the gold mixed-valence complexes, $M_2[Au^IX_2][Au^{III}X_4]$ (M = Rb, Cs; X = Cl, Br, and I), having perovskite-type structure. In spite of the three dimensional perovskite-type structure, the charge transfer interaction between Au^I and Au^{III} in these complexes is two-dimensional. These complexes undergo the pressure-induced Au valence transition from the mixed valence state of $Au^{I,III}$ to the single valence state of Au^{II}, which is coupled with a structural phase transition. In the pressure region below the Au valence transition, these complexes show a metallic behavior, which would be attributed to a dynamic two-electron exchange between the Au^I and Au^{III} states (i.e. highly mobile bipolarons). The metallic cubic phase appearing commonly for these complexes under high pressure and high temperature can be obtained as a metastable phase even at ambient pressure and room temperature. Moreover, as a recent topic, I report the photo-induced Au valence transition for $Cs_2[Au^IBr_2][Au^{III}Br_4]$.

Mixed-valence metal complexes are attracting current interest due to their characteristic physical properties.[1,2] Among them, one-dimensional halogen-bridged mixed-valence platinum complexes such as $[Pt(en)_2][PtX_2(en)_2](ClO_4)_4$ (en = ethylendiamine; X = Cl, Br, and I) have been extensively studied both experimentally and theoretically from the viewpoints of one-dimensional electron system having strong electron–phonon interaction.[3—14] In these systems, the strong electron–phonon coupling stabilizes the alternation of the Pt^{II} and Pt^{IV} sites, via the relaxation of the bridging halogen atom. The mismatches of the valence alternation in these complexes can be regarded as non-linear excitations such as kink-solitons and polarons. These have attracted much attention and have been studied extensively,[18—32] since the discovery of pressure-induced effect[15] and photo-induced[16,17] effect on the non-linear excitations.

Gold mixed-valence complexes, $M_2[Au^IX_2][Au^{III}X_4]$ (M = K, Rb, Cs; X = Cl, Br, and I) (here after denoted as $M_2Au_2X_6$), are another example for the halogen-bridged mixed-valence complexes, which have a distorted perovskite-type structure. So far, the following $M_2Au_2X_6$ and related complexes have been reported; $Cs_2Au_2X_6$ (X = Cl, Br, and I),[33—36] $Cs_2Ag^IAu^{III}X_6$ (X = Cl, Br),[34,37] $Cs_2Ag_2Cl_6$,[38] $Rb_2Au_2X_6$ (X = Br, I),[39] $K_2Au_2I_6$,[37] $(NH_4)_2Au_2I_6$,[37] $CsAu_{0.6}Br_{2.6}$,[40] $Cs_{1.16}(AuBr_4)(AuBr_2)_{0.08}(Br_3)_{0.08}$.[41] In connection with these complexes, $Cs_2Au_2Cl_6$ was first synthesized by Wells in 1922.[33] It was described as astonishingly jet black in color, from which the existence of metal–metal interaction was considered. Its crystal structure was determined by Elliott and Pauling by means of powdered X-ray diffraction measurement in the 1930s.[34,35] Subsequently, the single crystal X-ray structural analysis was performed by Tindemans-v. Eijndhoven et al.[42] After that, these measurements were carried out for $Cs_2Au_2Cl_6$; high-pressure electrical resistivity,[43] high-pressure single-crystal X-ray diffraction,[44] high-pressure neutron diffraction,[45] ^{197}Au Mössbauer spectroscopy,[46] high-pressure ^{197}Au Mössbauer spectroscopy,[47,48] and X-ray absorption near-edge structure (XANES).[49]

In the second half of the 1980s, with the discovery of high-T_c superconductors such as $La_{2-x}Ba_xCuO_4$[50] and $Ba_{1-x}K_xBiO_3$,[51] mixed-valence systems having perovskite-type structure have become of great interest. In these systems, interesting physical properties such as superconductivity remarkably depend on the valence state and the crystal structure. For example, the valence state of Bi has been considered as an important factor for a comprehension of the physical properties of $Ba_{1-x}K_xBiO_3$ and $BaPb_{1-x}Bi_xO_3$ system. The insulating state of the host compound $BaBiO_3$ is explained by the charge disproportionation of the Bi cations (IV into III and V) which couples to lattice deformation of the stabilization of commensurate charge density waves. According to recent theory,[52—55] an unusual superconductor due to the Bose condensation of bipolarons is expected under some electron–phonon coupling constant, λ, while in the large limit of λ, a bipolaronic insulator occurs. The insulating $BaBiO_3$ is regarded as an on-site bipolaron system where the bipolarons form a three-dimensional lattice and localize at the Bi^{III} site.

It is worth noting that $M_2Au_2X_6$ (M = K, Rb, Cs; X = Cl, Br, and I) also have a mixed-valence system having perovskite-type structure. Their characteristic properties of crystal structure and mixed valency are quite similar to those of $BaBiO_3$. From these viewpoints, we have systematically investigated the crystal structure and physical properties of $M_2Au_2X_6$.[40,56—77]

In this paper, I review the investigations of the structural *P–T* phase diagram, the Au valence state and the charge transfer interaction, the pressure-induced and the photo-induced Au valence transition, the metastable cubic phase and the metallic mixed-valence phase for $M_2Au_2X_6$.

The contents of this paper are as follows. In Sect. 1, experimental details are described. In Sect. 2, I review the characteristic properties of crystal structure. In Sect. 3, I discuss the nature of the chemical bond in $[AuX_2]^-$ and $[AuX_4]^-$ from the analysis of single-crystal ^{197}Au Mössbauer spectra and discuss the anisotropy of Au^{I}–Au^{III} charge transfer interaction by means of single crystal reflectance spectra and EHMO calculation. In Sect. 4, I discuss the structural phase transition coupled with the Au valence transition for $Cs_2Au_2X_6$ (X = Cl, Br, and I) and $Rb_2Au_2I_6$ under high pressures. In Sect. 5, I describe the pressure-induced Au valence transition from the $Au^{I,III}$ state to the Au^{II} state by means of X-ray structural analysis, ^{197}Au Mössbauer spectroscopy and Raman spectroscopy. In Sect. 6, I describe the metastable cubic phase in $Cs_2Au_2I_6$. In these complexes, the cubic perovskite structure appearing at high pressure and high temperature can be obtained as a metastable phase even at room temperature and ambient pressure. In Sect. 7, as a recent topic, I report the persistent photo-induced Au valence transition for $Cs_2Au_2Br_6$. In Sect. 8, I discuss the metallic mixed-valence phase for $Cs_2Au_2X_6$, and propose the possibility of melting of the bipolaron lattices under high pressure.

1. Experimental

The Au mixed-valence complexes, $M_2Au_2X_6$ (M = Rb, Cs; X = Cl, Br, and I), were synthesized in the same way as reported in Refs. 39, 40, and 56. The single crystals were grown by a diffusion method using an H-type test tube. As a solvent, acetonitrile and 55% hydroiodic acid were used for $Cs_2Au_2X_6$ (X = Cl, Br) and $M_2Au_2I_6$ (M = Rb, Cs), respectively. The bases of the two arms of H-tube were kept at 45 and 20 °C, respectively.

The *P–T* phase diagram of $M_2Au_2X_6$ was determined by the energy-dispersive X-ray diffraction method using a high-temperature and high-pressure apparatus called MAX90 with synchrotron radiation (SR) in High Energy Accelerator Research Organization (Tsukuba). The high-pressure apparatus is a cubic anvil type whose anvils compress a boron–epoxy cube containing a Teflon® capsule in which powdered sample and kerosene as a fluid pressure medium are packed. The pressure was determined by measuring the lattice constants of NaCl set in the boron–epoxy cube.

In the case of $Cs_2Au_2Cl_6$, single crystal X-ray analysis under high pressures up to 18 GPa was carried out by using a four circle diffractometer with a Merill–Bassett type diamond anvil cell, in Marburg University. Helium gas was used as the best hydrostatic pressure medium. The applied pressure was determined by using the luminescence peak of a small piece of ruby placed in the gasket hole. The details of the experimental procedure were described elsewhere.[73]

Polarized reflectance spectra of $Cs_2Au_2X_6$ (X = Cl, Br, and I) and $Rb_2Au_2I_6$ were measured at room temperature for the (110) and (001) faces. The (110) and (001) faces of $M_2Au_2X_6$ were confirmed by using a four-circle X-ray diffractometer. Only as grown surfaces were measured, and the absolute reflectivity was calibrated with an aluminium mirror.

A Mössbauer spectroscopic measurement of the 77.34 keV transition in ^{197}Au was carried out with both source and absorber cooled down to 16 K. A ^{197}Pt source was obtained by neutron irradiation of 98% enriched ^{196}Pt metal by the nuclear reaction $^{196}\mathrm{Pt}(n,\gamma)\ ^{197}\mathrm{Pt}$ in the Kyoto University Reactor. The isomer shift data were given with respect to gold in platinum metal at 16 K. The ^{197}Au Mössbauer spectroscopic measurements under low temperature and high pressures up to 12.5 GPa were carried out in Marburg University. Powdered samples mixed with wax were placed in a pyrophyllite sample holder located between two B_4C anvils mounted in a Cu–Be clamp system. The pressure at the sample was determined by using the known critical dependence of the transition of metallic to superconducting lead. A ^{197}Pt source with an activity of about 200 mCi was used. For this, a foil of ^{196}Pt (97% enriched) was exposed to a flux of neutrons at the Hahn Meitner Institute, Berlin, during 24 h. The experimental details were described elsewhere.[66]

The single crystal resistivity of $Cs_2Au_2Cl_6$ was measured by standard four probe method using a low-temperature and high-pressure apparatus in the Institute of Solid State Physics, University of Tokyo. The high-pressure apparatus is a cubic anvil type which compresses a pyrophyllite cube containing a Teflon® capsule. A mixture of Fluorinert (FC70 and FC77) was used as a fluid pressure medium. Sharp changes in the electrical resistivity of Bi_{I-II} (2.55 GPa), Bi_{II-III} (2.7 GPa), and Bi_{III-V} (7.7 GPa) were used to calibrate the pressure in the sample capsule.

High-pressure Raman spectroscopic measurements were carried out using a diamond anvil cell and liquid paraffin as a pressure medium, in Nagoya University. The applied pressure was monitored using the luminescence peak of a small piece of ruby placed in the gasket hole. The sample was excited at 514.5 nm with an argon ion laser in a backward configuration. The experimental details were described elsewhere.[75—77]

2. Crystal Structure

The crystal structures of $M_2Au_2X_6$ are shown in Fig. 1. In the crystal, all the halogens are distorted from the midpoint between neighboring Au ions in the chains, and the linear $[Au^{I}X_2]^-$ and square-planar $[Au^{III}X_4]^-$ complexes occur alternately. Consequently, their structures consist of three-dimensional metal-halogen frame-works formed by elongated octahedra with Au^{III} and compressed octahedra with Au^{I} sharing their corners. In other words, the breathing-mode-type distortion of AuX_6 octahedra is present in this system. The crystal data and tolerance factor (*t*) are listed in Table 1.[37,39,42,71] $K_2Au_2X_6$ (X = Cl, Br) and $Rb_2Au_2Cl_6$ have not yet been obtained.

The stability of the perovskite structure (ABX_3) depends

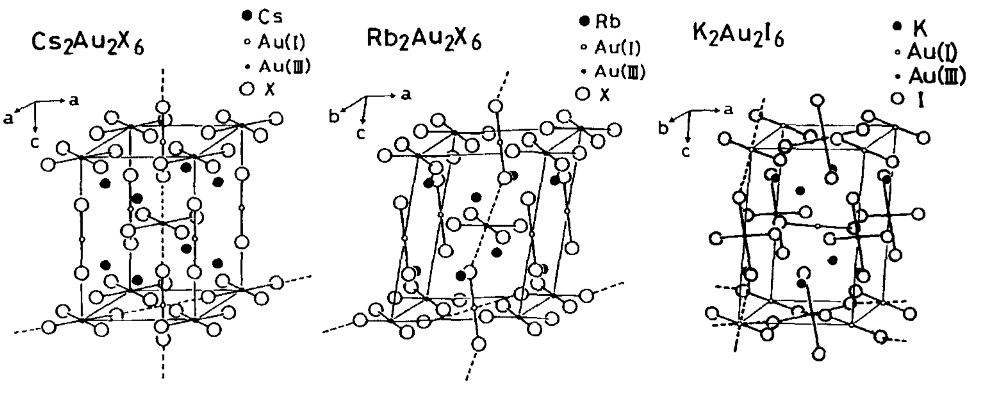

Fig. 1. Crystal structures of $Cs_2Au_2X_6$ (X = Cl, Br, and I), $Rb_2Au_2X_6$ (X = Br, I), and $K_2Au_2I_6$.

Table 1. Crystal Data and Tolerance Factor of $M_2Au_2X_6$ (M = K, Rb, Cs; X = Cl, Br,I)

Compound	Lattice system	Space group	Lattice parameters				$t^{a)}$
			a/Å	b/Å	c/Å	β/°	
$K_2Au_2I_6$	Monoclinic	$P2_1/n$	7.283(3)	9.259(3)	11.587(5)	93.0(1)	0.842
$Rb_2Au_2Br_6$	Monoclinic	$I2/m$	8.520(1)	7.243(1)	11.210(3)	101.24(5)	0.872
$Rb_2Au_2I_6$	Monoclinic	$I2/m$	8.725(2)	7.932(1)	11.969(4)	99.53(2)	0.860
$Cs_2Au_2Cl_6$	Tetragonal	$I4/mmm$	7.495(1)	$= a$	10.880(2)	90	0.920
$Cs_2Au_2Br_6$	Tetragonal	$I4/mmm$	7.759(1)	$= a$	11.308(1)	90	0.910
$Cs_2Au_2I_6$	Tetragonal	$I4/mmm$	8.284(1)	$= a$	12.092(2)	90	0.895

a) t denotes a tolerance factor defined by $r_A + r_X = t\sqrt{2}(r_B + r_X)$, where r_A, r_B, and r_X are the ionic radii of a cation of A-site, another cation of B-site, and an anion, respectively.

on the relative sizes of the A and B elements as well as on the electronic configuration of the B site ions. The size factor is expressed by a tolerance factor (t) obtained by considering the structure as derived from a close-packed stacking of the A and X ions. It is generally defined by the relationship $R_A + R_X = t\sqrt{2}(R_B + R_X)$, where R_A, R_B, and R_X are the ionic radii. In this relation, the ideal close packing corresponds to $t = 1$. The perovskite structure is found for t values between 0.8 and 1.1. In the cases of $Rb_2Au_2X_6$ (X = Br, I) and $K_2Au_2X_6$, because of the small values of t, the crystal structures are distorted into monoclinic and the tilting system of AuX_6 octahedra appears.

3. Gold Valence State in $M_2Au_2X_6$

3.1 Chemical Bond of Au–X in $[Au^IX_2]^-$ and $[Au^{III}X_4]^-$. The relativistic effect, which is strongest at the position of gold in the periodic table of elements, enormously stabilizes the 6s level and destabilizes the 5d levels of Au ($Xe4f^{14}5d^{10}6s^1$).[78] According to a recent MO calculation including the relativistic effect, the 5d6s hybridization rather than 6s6p hybridization is dominant for the chemical bonds in the linear $[Au^IX_2]^-$ complexes.[78,79] However, many studies of ^{197}Au Mössbauer spectra of gold(I) complexes have been interpreted in terms of sp hybridization of Au^I,[80—82] since the sign of electric field gradient (EFG) of Au^I in $KAu(CN)_2$ was determined to be negative.[83]

In order to elucidate this entangled problem, our group has investigated the sign of EFG of Au^I and Au^{III} in $Cs_2Au_2I_6$ by means of single crystal ^{197}Au Mössbauer spectroscopy.[67] The determination of the sign of EFG is one of the most powerful methods to investigate the nature of chemical bonds of Au–X in $[Au^IX_2]^-$. In the case of $[Au^IX_2]^-$, the $5d_{z^2}$ hole due to 5d6s hybridization produces a positive contribution to EFG, while the 6p_z electron due to 6s6p hybridization produces a negative one. On the other hand, in the case of square-planar $[Au^{III}X_4]^-$, the two electron holes in the $5d_{x^2-y^2}$ orbital produce a negative contribution to EFG, while the partly filled $5d6s6p^2$ hybrid yields a positive one.

Figures 2(a) and 2(b) show the ^{197}Au Mössbauer spectra of the powdered crystal and the single crystal of $Cs_2Au_2I_6$, respectively. As shown in Fig. 2(a), the best fit is obtained with two doublets, the outer with lower intensity being assigned to Au^I, the inner to Au^{III}. In the case of the powdered crystal, the intensity ratio, $I(Au^I)/I(Au^{III})$, is 0.72, which is due to the difference between the recoil-free fractions of Au^I and Au^{III}. Since the Au^I is in two-fold (linear) ligand coordination and the Au^{III} in four-fold (square-planar) coordination, the environment of the Au^{III} in $Cs_2Au_2I_6$ is more rigid than that of the Au^I. However, as shown in Fig. 2(b), $I(Au^I)/I(Au^{III})$ of the single crystal is 1.56, which implies that the recoil-free fraction along the molecular axis of $[Au^IX_2]^-$ is larger than that perpendicular to the plane of $[Au^{III}X_4]^-$.

In the case of $Cs_2Au_2I_6$, the quadrupole splitting for Au^I and Au^{III} is given by $eqV_{zz}/2$, where q is the nuclear quadrupole moment ($+0.59\times10^{-28}$ m^2 for the ground state of ^{197}Au) and V_{zz} is the principal component of the EFG. Therefore, the concentration of negative charge in the xy plane makes EFG positive and the ground doublet becomes $I_z = \pm1/2$. On the other hand, the concentration of negative charge on the z-axis makes EFG negative and the ground

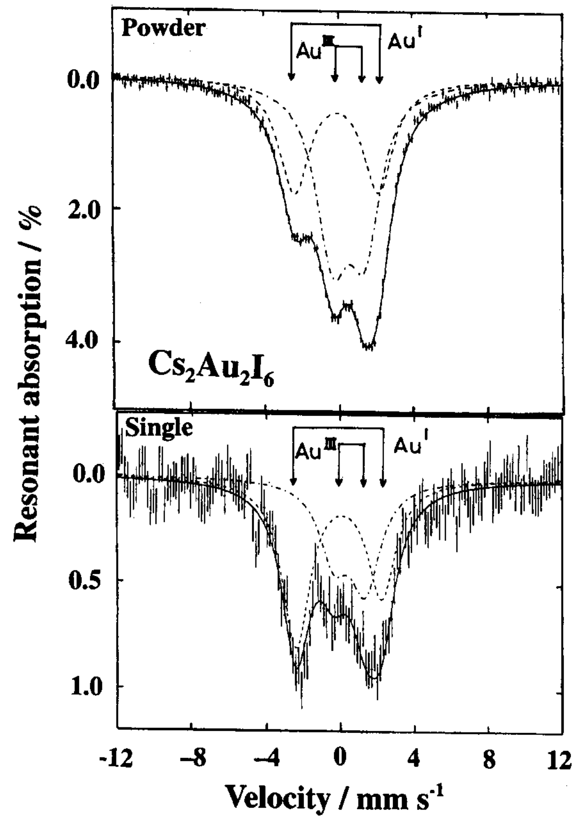

Fig. 2. ^{197}Au Mössbauer spectra of $Cs_2Au_2I_6$ at 16 K. (a) powdered crystal, (b) single crystal, $\gamma \| c$. Isomer shift is relative to gold in platinum (Ref. 67).

doublet becomes $I_z = \pm 3/2$. In the case of ^{197}Au, the 77.34 keV transition is a mixture of magnetic dipole transition (M1) and electric quadrapole transition (E2) with mixing ratio $E2/M1 \equiv \delta = -0.352 \pm 0.005$.[83] Taking account of the M1–E2 mixing, one may express the intensity ratio as follows,[83]

$$I(\pm 3/2 \rightarrow \pm 1/2)/I(\pm 1/2 \rightarrow \pm 1/2) = \{2(\sqrt{3}+\delta)^2 - 3(1+2\sqrt{3}\delta - \delta^2)\sin^2\theta\}/\{2(1-\sqrt{3}\delta)^2 + 3(1+2\sqrt{3}\delta - \delta^2)\sin^2\theta\}. \quad (1)$$

In our experiment, the direction of the incident γ-rays is parallel to the c-axis (i.e. the axis of quantization) of $Cs_2Au_2I_6$. Therefore, when one takes account of the M1–E2 mixing, the intensity ratio of I ($\pm 3/2 \rightarrow \pm 1/2$)/$I$ ($\pm 1/2 \rightarrow \pm 1/2$) for $\theta = 0$ should be 0.735. In the case of $Cs_2Au_2I_6$, the intensity ratio between the weaker and the stronger branches is 0.69 and 0.71 for the Au^I and Au^{III} sites, respectively. These values are consistent with the theoretically predicted value. Comparing the obtained spectral profile of Fig. 2(b) with the theoretical transition probability ratio including the M1–E2 mixing, one can determine the signs of EFG for Au^I and Au^{III} in $Cs_2Au_2I_6$ to be negative and positive, respectively. The negative sign of EFG for Au^I in $Cs_2Au_2I_6$ is consistent with that for Au^I in $KAu(CN)_2$.[83]

From the ^{197}Au Mössbauer spectra, it is obvious that the contributions of $6p_z$ and $6p_{x,y}$ determine the sign of EFG for Au^I in $[Au^II_2]^-$ and for Au^{III} in $[Au^{III}I_4]^-$, respectively. However, this result can not exclude the existence of $5d6s$ mixing in $[Au^IX_2]^-$. Figures 3 and 4 show the schematic energy diagrams of $[Au^IX_2]^-$ and $[Au^{III}X_4]^-$, respectively, which are derived from extended Hückel molecular orbital calculation (EHMO). In Figs. 3 and 4, only the σ orbitals are picked up because the bonding of the halogeno complexes is predominantly σ in character. In the case of bonding in $[Au^IX_2]^-$, there are two main contributions to this. The first is due to the mixing of the halogen-p_z, Au-$5d_{z^2}$ and Au-$6s$ orbitals. In the absence of the Au-$6s$ mixing, the overlap between the halogen-p_z and Au-$5d_{z^2}$ would result in a bonding and antibonding pair of $1\sigma_g$ and $2\sigma_g$, and there would be no net bonding. The mixing with Au-$6s$ orbital, however, produces a stabilization of the $2\sigma_g$ orbital. The second is due to the overlap of the halogen-p_z and Au-$6p_z$ orbitals, which produces a stabilization of the nonbonding $1\sigma_u$ orbital. Note that both of the $6s$ and $6p_z$ orbitals contribute to the bonding in $[Au^IX_2]^-$, but these orbitals go into different molecular orbitals. In the case of $[Au^{III}X_4]^-$, as shown in Fig. 4, the $6s$ and $6p_{x,y}$ orbitals of Au go into the $1a_{1g}$ and $1e_u$ molecular orbitals and stabilize them.

3.2 Charge Transfer Interaction between Au^I and Au^{III}. In $M_2Au_2X_6$, as pointed out by Robin and Day,[84] there are two relative orientations between $[Au^IX_2]^-$ and

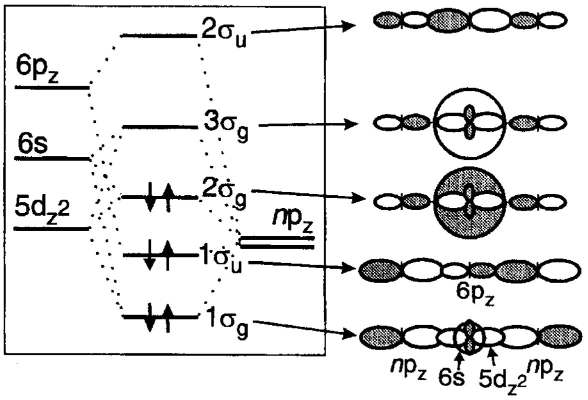

Fig. 3. Schematic MO correlation diagram for a linear complex, $[Au^IX_2]^-$.

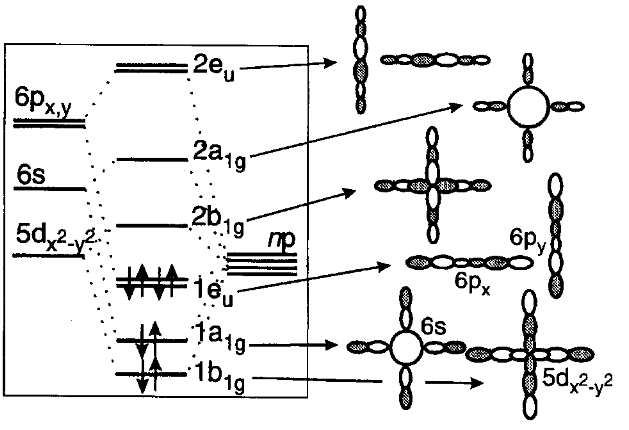

Fig. 4. Schematic MO correlation diagram for a square planar complex, $[Au^{III}X_4]^-$.

$[\mathrm{Au^{III}X_4}]^-$. In one, the ····X–Au$^{\mathrm{I}}$–X····Au$^{\mathrm{III}}$····X–Au$^{\mathrm{I}}$–X···· network lies along the *c*-axis, while in the other, the ····X–Au$^{\mathrm{III}}$–X····Au$^{\mathrm{I}}$····X–Au$^{\mathrm{III}}$–X···· network lies in the *ab* plane. However, as to which of these configurations is dominant in the charge-transfer interaction between the Au$^{\mathrm{I}}$ and Au$^{\mathrm{III}}$ ions has been a matter of debate.

Figures 5 and 6 show the single crystal reflectance spectra of $\mathrm{Cs_2Au_2I_6}$ and $\mathrm{Rb_2Au_2I_6}$, respectively. In both cases, the reflectance spectra for $\boldsymbol{E}\perp c$ is remarkably stronger than that for $\boldsymbol{E}\parallel c$ in the lower energy region. In particular, the strongest reflectance peak at the lowest energy region is observed only for $\boldsymbol{E}\perp c$, which implies that this reflection peak corresponds to the inter-valence charge transfer (IVCT) from the Au$^{\mathrm{I}}$ ($5d_{x^2-y^2}$) orbital to the Au$^{\mathrm{III}}$ ($5d_{x^2-y^2}$) orbital within the Au–X network in the *ab* plane. From the group theoretical analysis, the selection rule of the IVCT from Au$^{\mathrm{I}}$ to Au$^{\mathrm{III}}$ in $\mathrm{M_2Au_2X_6}$ is shown in Fig. 7. Considering the energy diagram of the 5*d* orbitals of Au$^{\mathrm{I}}$ and Au$^{\mathrm{III}}$ and overlapping integral between these orbitals, one may assign the IVCT bands in $\mathrm{Cs_2Au_2I_6}$ to the following transitions. IVCT at 11000 cm^{-1}: Au$^{\mathrm{I}}$ ($5d_{x^2-y^2}$)→Au$^{\mathrm{III}}$ ($5d_{x^2-y^2}$), IVCT at 14500 cm^{-1}: Au$^{\mathrm{I}}$ ($5d_{yz,zx}$)→Au$^{\mathrm{III}}$ ($5d_{x^2-y^2}$), IVCT at 16000 cm^{-1}: Au$^{\mathrm{I}}$ ($5d_{xy}$)→Au$^{\mathrm{III}}$($5d_{x^2-y^2}$). As shown in Fig. 7, the lowest IVCT band corresponds to the Au$^{\mathrm{I}}$ ($5d_{z^2}$)→Au$^{\mathrm{III}}$ ($5d_{x^2-y^2}$) transition, but the overlap between these orbitals is small. A weak band corresponding to this IVCT would be observed on the lower energy side of the IVCT band at 11000 cm^{-1} for the $\boldsymbol{E}\perp c$ polarization. Recently, Kitagawa et al.[85] have observed a weak shoulder at ca. 6500 cm^{-1} in the single-crystal reflectance spectra in $\mathrm{Cs_2Au_2I_6}$ for the $\boldsymbol{E}\perp c$ polarization. This weak shoulder seems to correspond to the Au$^{\mathrm{I}}$ ($5d_{z^2}$)→Au$^{\mathrm{III}}$ ($5d_{x^2-y^2}$) transition. From this fact, one concludes that the charge transfer interaction between the $5d_{x^2-y^2}$ orbitals of Au$^{\mathrm{I}}$ and Au$^{\mathrm{III}}$ in the *ab* plane is dominant for the IVCT bands in $\mathrm{M_2Au_2X_6}$. Figure 8 shows the polarized reflectance spectra for $\mathrm{Cs_2Au_2X_6}$(X = Cl, Br, and I). As shown in Fig. 8, the energies of both the IVCT bands are in the order $\mathrm{Cs_2Au_2Cl_6} > \mathrm{Cs_2Au_2Br_6} > \mathrm{Cs_2Au_2I_6}$, indicating that the energy difference between the electronic states of Au$^{\mathrm{I}}$ and Au$^{\mathrm{III}}$ becomes smaller from X = Cl to I.

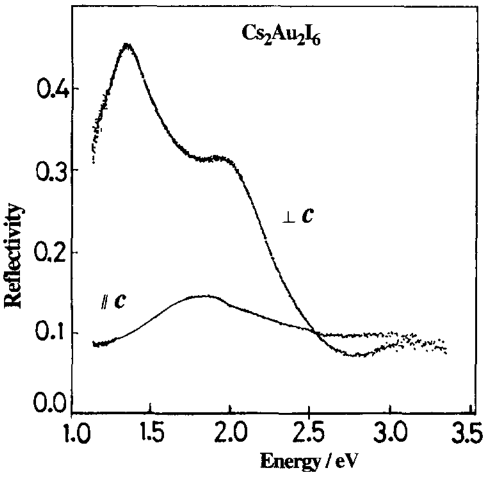

Fig. 5. Polarized single-crystal reflectance spectra of $\mathrm{Cs_2Au_2I_6}$ at room temperature. $\boldsymbol{E}\perp c$ and $\boldsymbol{E}/\!/c$. $\boldsymbol{E}$ denotes the electric vector of the incident light.

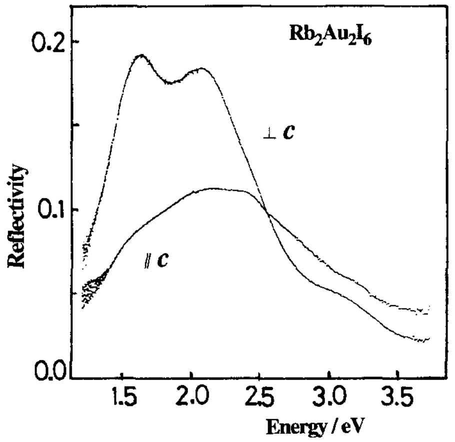

Fig. 6. Polarized single-crystal reflectance spectra of $\mathrm{Rb_2Au_2I_6}$ at room temperature. $\boldsymbol{E}\perp c$ and $\boldsymbol{E}/\!/c$. $\boldsymbol{E}$ denotes the electric vector of the incident light.

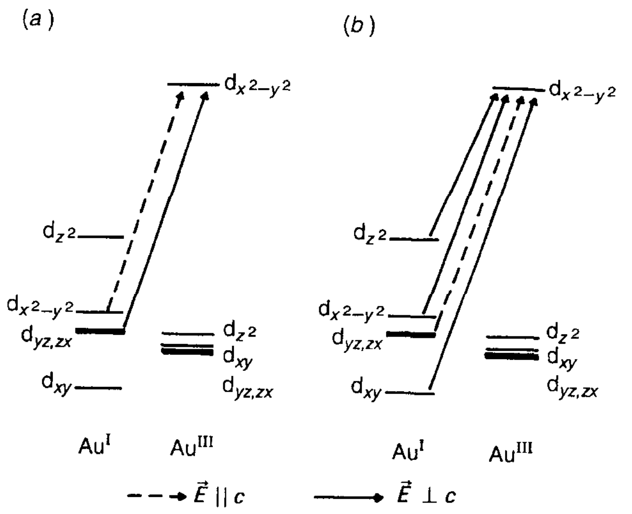

Fig. 7. Selection rules of the IVCT transitions for $\mathrm{Cs_2Au_2X_6}$. (a) Along the *c* axis and (b) in the *ab* plane; $\boldsymbol{E}$ denotes the electric vector of the incident light. The schematic energy levels of the compressed $\mathrm{Au^IX_6}$ and the elongated $\mathrm{Au^{III}X_6}$ octahedra in $\mathrm{Cs_2Au_2X_6}$ are derived from extended-Hückel molecular orbital calculation.

As mentioned above, it is obvious that the charge transfer interactions between Au$^{\mathrm{I}}$ and Au$^{\mathrm{III}}$ in $\mathrm{M_2Au_2X_6}$ are two-dimensional. In connection with this, as shown in Fig. 9, there are two possible charge transfer interactions between Au$^{\mathrm{I}}$ and Au$^{\mathrm{III}}$ in the *ab* plane. The polarized reflectance spectra imply that the Au$^{\mathrm{I}}$ ($5d_{x^2-y^2}$)→Au$^{\mathrm{III}}$ ($5d_{x^2-y^2}$) interaction is predominant. Strictly speaking, $e\int\phi^*$ (Au$^{\mathrm{III}}$ ($5d_{x^2-y^2}$)) $\boldsymbol{r}$ ϕ (Au$^{\mathrm{I}}$ ($5d_{x^2-y^2}$)) $d\tau$ is predominant for the IVCT transition in $\mathrm{M_2Au_2X_6}$.

On the other hand, the ground state wavefunction can be expressed as follows,

$$\Psi = (1-\alpha^2)^{1/2}\{\phi_i(\mathrm{Au^I})\phi_j(\mathrm{Au^{III}})\} + \alpha\{\phi_i(\mathrm{Au^{III}})\phi_j(\mathrm{Au^I})\}, \quad (2)$$

where, α, called the "valence delocalization coefficient",

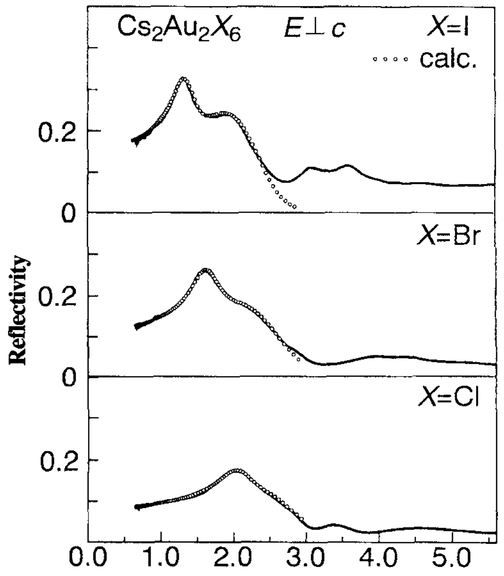

Fig. 8. Polarized single-crystal reflectance spectra ($E \perp c$) of $Cs_2Au_2X_6$ (X = Cl, Br, and I) at room temperature. Open circles are the best-fitted results with a two-Lorentz oscillator model (Ref. 74).

denotes the degree of the charge transfer interaction and is approximately expressed as $H_{ij}/(E_j - E_i)$. Here, H_{ij} denotes the transfer integral between ϕ_i (Au$^{\rm I}$) and ϕ_j (Au$^{\rm III}$). Since the smallest energy separation is between the Au$^{\rm I}$ ($5d_{z^2}$) and Au$^{\rm III}$ ($5d_{x^2-y^2}$) orbitals, the valence delocalization parameter, α, may be predominant even if the transfer integral, H_{ij}, between Au$^{\rm I}$ ($5d_{z^2}$) and Au$^{\rm III}$ ($5d_{x^2-y^2}$) is smaller than that between Au$^{\rm I}$ ($5d_{x^2-y^2}$) and Au$^{\rm III}$ ($5d_{x^2-y^2}$). In order to elucidate the predominant charge transfer interaction in the ground state of $M_2Au_2X_6$, I calculated the valence delocalization parameter between Au$^{\rm I}$ and Au$^{\rm III}$ in $Cs_2Au_2I_6$ by means of the EHMO method. For simplicity, I calculated the molecular orbitals in the $[Au^{I}I_2]^-[Au^{III}I_4]_6^-$ cluster, where the $[Au^{I}I_2]^-$ ion is surrounded by the six $[Au^{III}I_4]^-$ ions. Figures 10(a) and 10(b) show the pressure dependence of the square of the coefficient of ϕ(Au$^{\rm III}$ ($d_{x^2-y^2}$)) in the molecular orbitals, based on the Au$^{\rm I}$ (d_{z^2}) and Au$^{\rm I}$ ($d_{x^2-y^2}$) orbitals, respectively. As shown in Fig. 10, the valence delocalization parameter between Au$^{\rm I}$ (d_{z^2}) and Au$^{\rm III}$ ($d_{x^2-y^2}$) is predominant for the ground state of $Cs_2Au_2X_6$, which is strongly supported by the pressure dependence of the isomer shifts of Au$^{\rm I}$ and Au$^{\rm III}$ in ^{197}Au Mössbauer spectra of $Cs_2Au_2Cl_6$.[48] Note that, as pointed out by Orgel,[86] the ds hybridized orbital, $(1/\sqrt{2})$-$(5d_{z^2} - 6s)$, spreads out in the xy plane. As shown in Fig. 3, the highest occupied orbital ($2\sigma_g$) of $[Au^{I}X_2]^-$, where the sign of the coefficient of $6s$ is opposite to that of $5d_{z^2}$, spreads out in the xy plane, which would be responsible for the large delocalization parameter between Au$^{\rm I}$ (d_{z^2}) and Au$^{\rm III}$ ($d_{x^2-y^2}$) in the ab plane in $Cs_2Au_2X_6$.

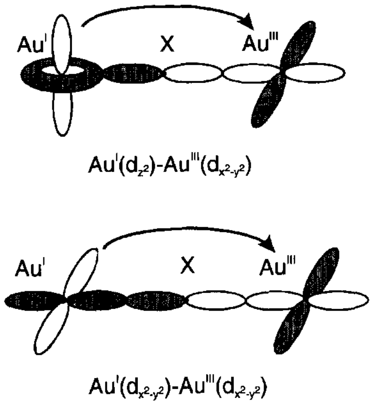

Fig. 9. Two types of charge transfer interaction between Au$^{\rm I}$ and Au$^{\rm III}$ in $M_2Au_2X_6$.

In order to precisely determine the delocalization parameter, α, a detailed orbital calculation based on the density functional method is in progress.

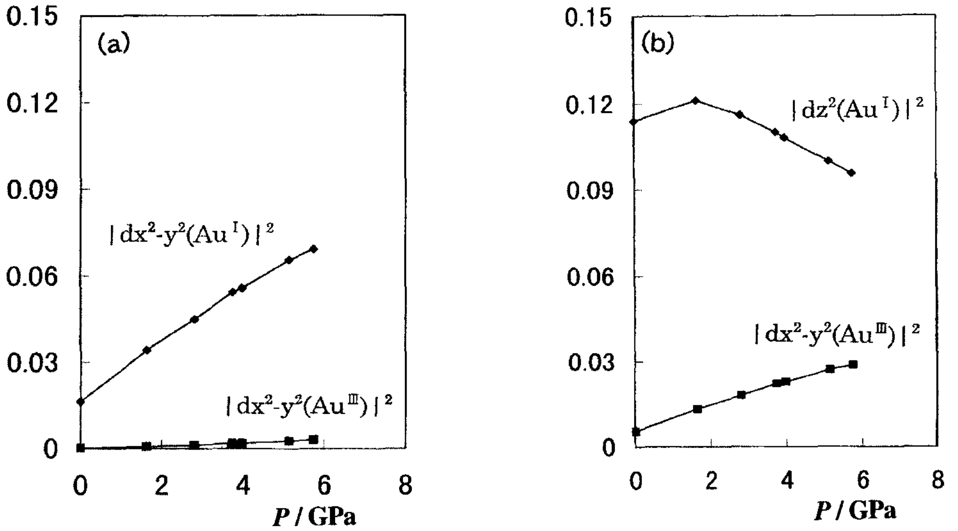

Fig. 10. (a) Pressure dependence of the coefficient of the Au$^{\rm III}$ atomic orbital ($5d_{x^2-y^2}$) in the molecular orbital Ψ (Au$^{\rm I}$-$5d_{x^2-y^2}$) for $Cs_2Au_2I_6$. (b) Pressure dependence of the coefficient of the Au$^{\rm III}$ atomic orbital ($5d_{x^2-y^2}$) in the molecular orbital Ψ (Au$^{\rm I}$-$5d_{z^2}$) for $Cs_2Au_2I_6$.

4. Pressure Induced Phase Transition

Investigations of the structural and the electronic properties of $Cs_2Au_2Cl_6$ under high pressures were started from 1974. Keller et al. reported a strong continual decrease in the electrical resistivity by nearly nine orders of magnitude from ambient pressure to 12 GPa. A gradual semiconductor-to-metal transition at room temperature and 6.5 GPa has been interpreted as evidence for the overlap of the filled $5d_{z^2}$ band of Au^{I} and the empty $5d_{x^2-y^2}$ one of Au^{III}.[43] Being stimulated by this phenomenon, Denner et al. carried out the single crystal X-ray diffraction measurement for $Cs_2Au_2Cl_6$ under high pressures.[44] According to them, with increasing pressure, the Cl atom shifts gradually toward the midpoint of the Au atoms that is attained at 5.2 GPa. Therefore, they have proposed that the Au sites become indistinguishable and the valence state of Au is Au^{II} above 5.2 GPa. However, ^{197}Au Mössbauer spectra[47,48] and Raman spectra[49] of $Cs_2Au_2Cl_6$ under high pressures have shown that the Au^{I} and Au^{III} sites are clearly distinguishable even at 6.8 and 8.0 GPa, respectively.

Recently, we have performed the single crystal X-ray diffraction for $Cs_2Au_2Cl_6$ under high pressures up to 18 GPa by using He gas as a pressure medium,[73] and have detected the superstructure reflections (*hkl*; l = odd) due to the shift of the Cl ions from the midpoint of the Au ions even at 12.0 GPa. These superstructure reflections disappeared at the structural phase transition ($P \approx 12$ GPa). As shown in Fig. 11, at about 12 GPa, the lattice parameters a and c approach each other, resulting in the relation $\sqrt{2}a = c$. It is therefore concluded that the crystal structure changes from tetragonal (*I4/mmm*) to cubic (*Pm3m*) at about 12 GPa. This result is not consistent with that of the previous powder X-ray diffraction measurement.[64] According to the powder X-ray diffraction measurement,[64] $Cs_2Au_2Cl_6$ undergoes a tetragonal-to-tetragonal phase transition at about 11—12 GPa and room temperature, and undergoes a tetragonal-to-cubic phase transition above 12 GPa and 373 K. It should be noted that the cubic phase exists even at room temperature under high pressures on condition that He gas is used as an ideal hydrostatic pressure medium. In the case of the previous powder X-ray diffraction measurement, the pressure medium was kerosene, which is not a good hydrostatic medium under high pressure, and the shearing stress might be responsible for the appearance of the second tetragonal phase in $Cs_2Au_2Cl_6$. The crystal structure of the phase II in $Cs_2Au_2X_6$ is very sensitive to the kind of pressure medium.

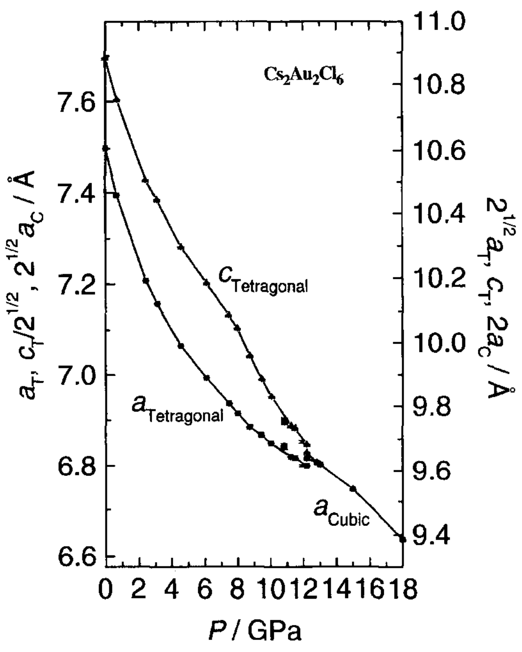

Fig. 11. Pressure dependence of the lattice parameters for $Cs_2Au_2Cl_6$ at room temperature (Ref. 73).

Figure 12 shows the phase diagram for $Cs_2Au_2X_6$ (X = Cl, Br, and I) and $Rb_2Au_2I_6$ under high pressures. In Fig. 12, T, C, and M denote the tetragonal, cubic, and monoclinic phases, respectively. The phase marked by slant lines has the single valence state of Au^{II}. The pressure induced phase transitions in $Cs_2Au_2X_6$ (X = Cl, Br, and I) are of first order. In the case of $Rb_2Au_2I_6$, on the other hand, a monoclinic and three kinds of tetragonal phases exist. In this complex, the pressure induced phase I (M) – phase II (T(I)) and the phase III (T(II)) – phase IV (T(III)) transitions are of first order, while the phase II (T(I)) – phase III (T(II)) is of second order.

5. Gold Valence Transition

5.1 X-Ray Structural Analysis. As mentioned in Sect. 4, at room temperature, $Cs_2Au_2Cl_6$, $Cs_2Au_2Br_6$ and $Cs_2Au_2I_6$ undergo a pressure induced structural phase transition at 11—12, 9, and 5.5 GPa, respectively, whose values are beyond the pressure where the activation energy for the electrical resistivity becomes zero. The pressures where the activation energies become zero are 7.5, 7.2, and 4.4 GPa, for $Cs_2Au_2Cl_6$, $Cs_2Au_2Br_6$, and $Cs_2Au_2I_6$, respectively.[57] Above the pressure where the activation energy becomes zero, the difference between the real oxidation states of Au^{I} and Au^{III} becomes quite small, which is proved by the fact that the (211) and (103) reflections, caused by the distortion of the bridging halogens from the midpoint between the Au^{I}

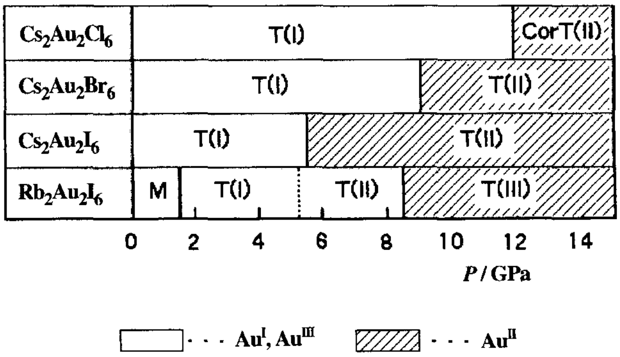

Fig. 12. Phase diagram of $Cs_2Au_2X_6$ (X = Cl, Br, and I) and $Rb_2Au_2I_6$. M: monoclinic, T: tetragonal, C: cubic. In the second phase in $Cs_2Au_2Cl_6$, the cubic phase appears by using He gas as a pressure medium, while the tetragonal (II) phase appears by using kerosene as a pressure medium.

and Au^{III} ions, are hardly detected in this pressure region. If the valence states of Au^{I} and Au^{III} finally become Au^{II} ($5d^9$), the lowering in symmetry of AuX_6 octahedra should be caused by the Jahn–Teller effect. In the case of $Cs_2Au_2I_6$, as shown in Fig. 13, $\sqrt{2}a/c$ increases from 0.969 to 0.980 with increasing pressure up to about 5.5 GPa. However, it drops abruptly from 0.980 to 0.970 at about 5.5 GPa. The abrupt drop in $\sqrt{2}a/c$ of $Cs_2Au_2I_6$ can be attributed to the band Jahn–Teller transition caused by realization of the Au^{II} valence state.

Above the transition pressure, $\sqrt{2}a/c$ of $Cs_2Au_2I_6$ is smaller than 1.0 and the value decreases with increasing pressure, which implies that the AuI_6 octahedra of $Cs_2Au_2I_6$ are elongated. Considering the distortion of the AuI_6 octahedra in $Cs_2Au_2I_6$, the HOMO in the second tetragonal phase is the half-filled $5d_{x^2-y^2}$. Therefore, the phase II in $Cs_2Au_2I_6$ behaves as a two-dimensional conductor. As expected from the high-pressure X-ray analysis, the behavior of the electrical conductivity in the phase II of $Cs_2Au_2I_6$ is highly anisotropic and two-dimensional.[61]

On the other hand, as shown in Fig. 14, $\sqrt{2}a/c$ of $Cs_2Au_2Cl_6$ increases remarkably with pressure above 8 GPa and it reaches to 1.0 at the transition pressure, which implies that the $AuCl_6$ octahedra in the phase II of $Cs_2Au_2Cl_6$ are regular octahedra. In the case of d^9 configuration, according to Pryce et al.,[87] the degree of elongation in the Jahn–Teller distorted octahedron, MX_6, decreases with decreasing the covalency between the central metal and the ligand. In fact, the compressed octahedra induced by Jahn–Teller effect have been observed for a few compounds (e.g. $KCuAlF_6$,[88] $KCu_3(OH)_2[(AsO_4)H(AsO_4)]$,[89] $CsAgMF_6$ (M = Sc, In, and Tl),[90] etc.), where the difference in the electronegativity between the central metal and the ligand is large. In the case of $Cs_2Au_2X_6$, the difference in the electronegativity between Au and X is 0.6, 0.4, and 0.1 for X = Cl, Br, and I, respectively. Therefore, the AuI_6 octahedra in the phase II of $Cs_2Au_2I_6$ may be elongated, while the $AuCl_6$ in the phase II of $Cs_2Au_2Cl_6$ may accidentally be non-distorted. If $Cs_2Au_2F_6$ is synthesized in future, the AuF_6 octahedra in the single valence phase would be compressed.

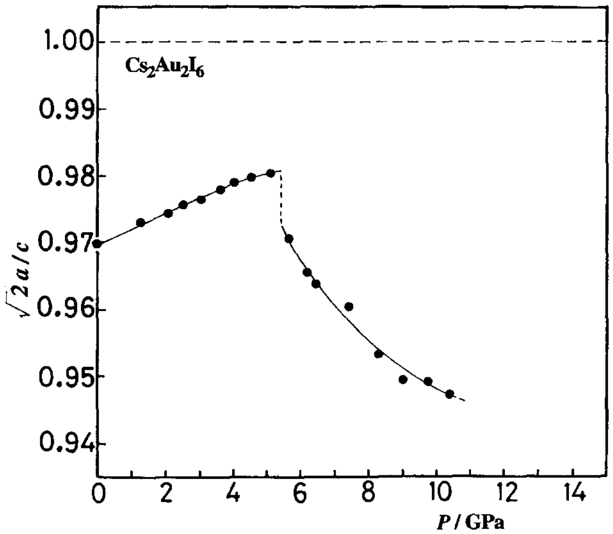

Fig. 13. Pressure dependence of the axial ratio $\sqrt{2}a/c$ of $Cs_2Au_2I_6$ (Ref. 64).

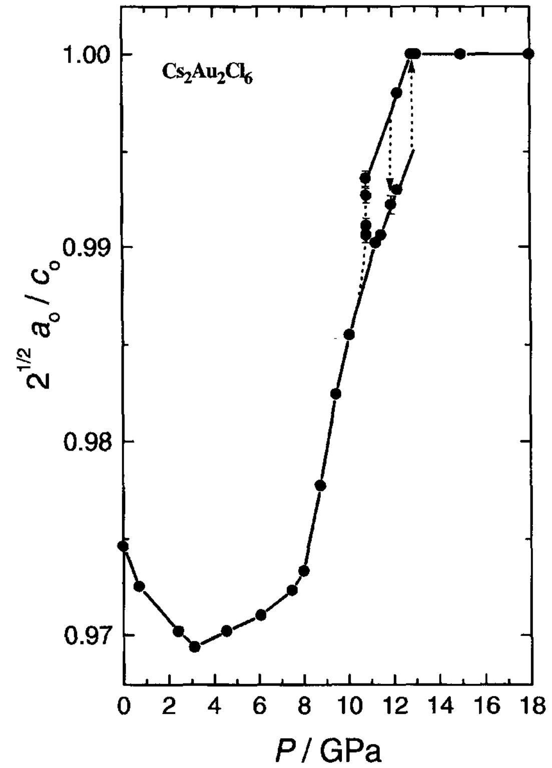

Fig. 14. Pressure dependence of the axial ratio $\sqrt{2}a/c$ of $Cs_2Au_2I_6$ (Ref. 73).

5.2 ^{197}Au Mössbauer Spectroscopy. As mentioned above, from the X-ray structural analysis, I have concluded that the pressure-induced structural phase transition from phase I to phase II in $M_2Au_2X_6$ is driven by the Au valence transition from the $Au^{I,III}$ state to the Au^{II} state. Our group has investigated the Au valence transition, more microscopically. ^{197}Au Mössbauer spectroscopy is one of the most powerful methods to investigate the Au valence state. Figure 15 shows the ^{197}Au Mössbauer spectra of $Cs_2Au_2I_6$ under high pressures up to 12.5 GPa.[66] The valence states of Au^{I} and Au^{III} at ambient pressure are clearly distinguishable. As shown in Fig. 15, with increasing pressure, a gradual increase in the overlap of the doublets is observed due to a substantial increase of the isomer shift of Au^{I} and a less pronounced decrease of that of Au^{III} with increasing pressure. Finally, the ^{197}Au Mössbauer spectrum at 12.5 GPa shows only one electronic state for Au in $Cs_2Au_2I_6$. Therefore, the Au valence state of the tetragonal(II) phase in $Cs_2Au_2I_6$ is concluded to be Au^{II}, which is the first direct observation of the Au^{II} state in a relatively simple, primarily ionic compound.

5.3 Raman Spectroscopy. Raman spectroscopy is also one of the most powerful methods to investigate the Au valence transition from the mixed valence state ($Au^{I,III}$) to the single valence state (Au^{II}). In the case of halogen-bridged mixed valence complexes, the symmetric stretching mode between the central metal atom and the bridging halogen

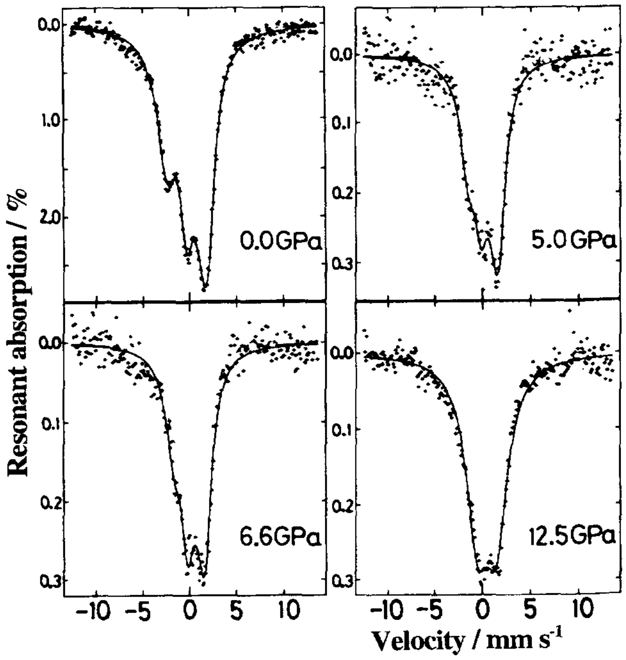

Fig. 15. Pressure dependence of the ^{197}Au Mössbauer spectra of $Cs_2Au_2I_6$ at 4.2K (Ref. 66). The isomer shift is relative to gold in platinum.

atom is strongly Raman active and shows a prominent resonance Raman effect by the incident light corresponding to the IVCT transition. The M–X stretching mode gives rise to a progressively less intense Raman band as the equilibrium position of the halogen atom moves toward the midpoint of the metal atoms. Eventually the stretching mode becomes Raman inactive when the halogen atoms are located at the midpoint of the metal atoms, i.e. when the single valence state is attained. This phenomenon is explained as follows. When the valence transition from the mixed valence state to the single valence state takes place, the unit cell size in the M–X direction becomes halved, where the M–X stretching mode at the Brillouin-zone center is converted to that at the Brillouin-zone boundary. Because of the $k = 0$ selection rule, the M–X stretching mode at the Brillouin-zone boundary becomes Raman inactive.

Figure 16 shows the Raman spectra for (a) $Cs_2Au_2Cl_6$ and (b) $Cs_2Au_2Br_6$ at ambient pressure.[75] Two A_{1g} modes are observed in the $c(a+b,a+b)\bar{c}$ configuration, while one B_{1g} mode is observed in the $c(a+b, a-b)\bar{c}$ configuration. Judging from the longer Au–Cl bond (2.295 Å) in the $[Au^{III}Cl_4]^-$ molecule as compared with the bond (2.281 Å) in the $[Au^{I}Cl_2]^-$ molecule, one may ascribe the lower-lying two modes, i.e. B_{1g} (297 cm^{-1}) and A_{1g} (299 cm^{-1}) modes, to the $[Au^{III}Cl_4]^-$ molecule. The higher-lying A_{1g} (324 cm^{-1}) mode is due to the $[Au^{I}Cl_2]^-$ molecule. Figure 17 shows the pressure dependence of the Raman spectra at 300 K for (a) $Cs_2Au_2Cl_6$ and (b) $Cs_2Au_2Br_6$. With increasing pressure, the intensities of the Raman-active A_{1g} and B_{1g} modes decrease, and eventually these modes disappear above 12.2 GPa for X = Cl and 7.5 GPa for X = Br, respectively. As mentioned above, the disappearance of the Raman-active modes indicates that the halogen atom shifts to the midpoint between the two neighboring Au atoms, i.e. the Au valence transition from the mixed-valence $Au^{I,III}$ state to the single-valence Au^{II} state takes place. In Fig. 18 are shown the pressure-dependence of the intensities of the B_{1g}modes for (a) $Cs_2Au_2Cl_6$ and (b) $Cs_2Au_2Br_6$ at 300 K. Open and closed circles show the data obtained in the pressure-increasing and pressure-decreasing runs, respectively. We defined the pressures where the intensity becomes half of the ambient pressure value as the critical pressures (indicated by arrows). *Pc,i* and *Pc,d* represent the critical pressures for the respective runs. The steep drop of the intensity as well as the prominent pressure-hysteresis (hatched region) indicates the first-order nature of the Au valence transition.

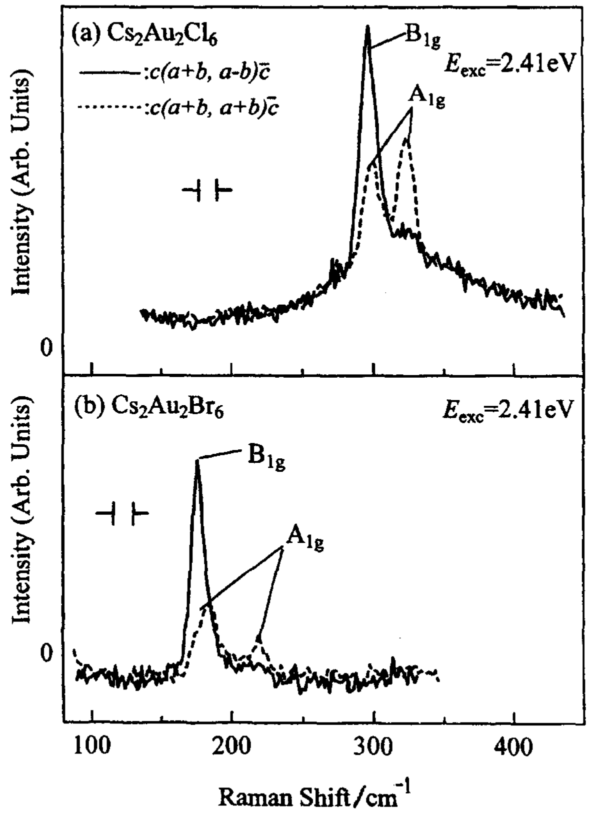

Fig. 16. Raman spectra for $Cs_2Au_2X_6$ at 300 K for (a) X = Cl and (b) X = Br. Solid and broken curves are the spectra with configurations of $c(a+b,a-b)\bar{c}$ and $c(a+b,a+b)\bar{c}$, respectively. Excitation energy E_{exc} is 2.41 eV (Ref. 75).

6. Cubic Phase and Its Metastable State

Now, we investigate the relationship between the *P–T* phase diagram and the transport phenomena. Figure 19 shows the *P–T* phase diagram of $Cs_2Au_2I_6$.[64] The mixture of two or three phases in the vicinity of the phase boundary is due to the non-equilibrium effect and the distribution of pressure and/or temperature in the sample. In the case of $Cs_2Au_2I_6$, two kinds of tetragonal phases and a cubic phase exist. The cubic phase commonly exists in the *P–T* phase of $Cs_2Au_2X_6$ (X = Cl, Br, and I) and $Rb_2Au_2I_6$.[69]

Figure 20 shows the pressure dependence of the elec-

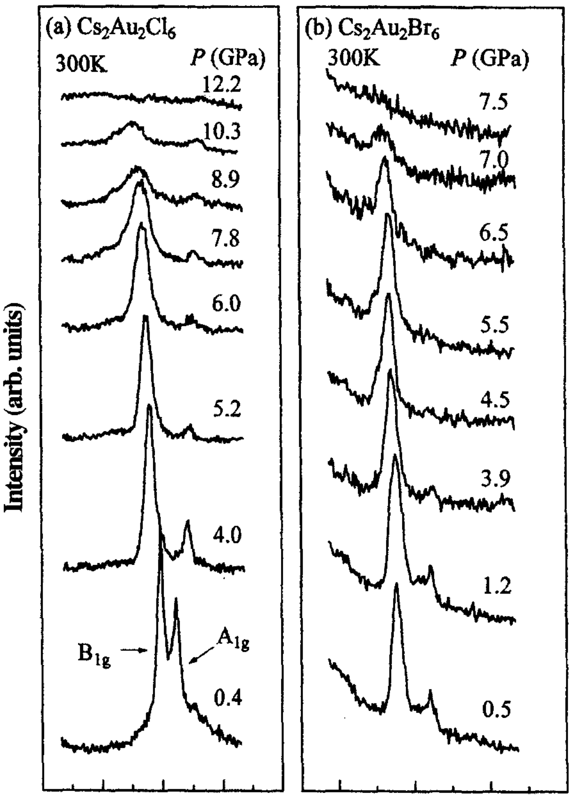

Fig. 17. Pressure dependence of the Raman spectra for (a) $Cs_2Au_2Cl_6$ and (b) $Cs_2Au_2Br_6$ at 300 K with unpolarized configuration (Ref. 75).

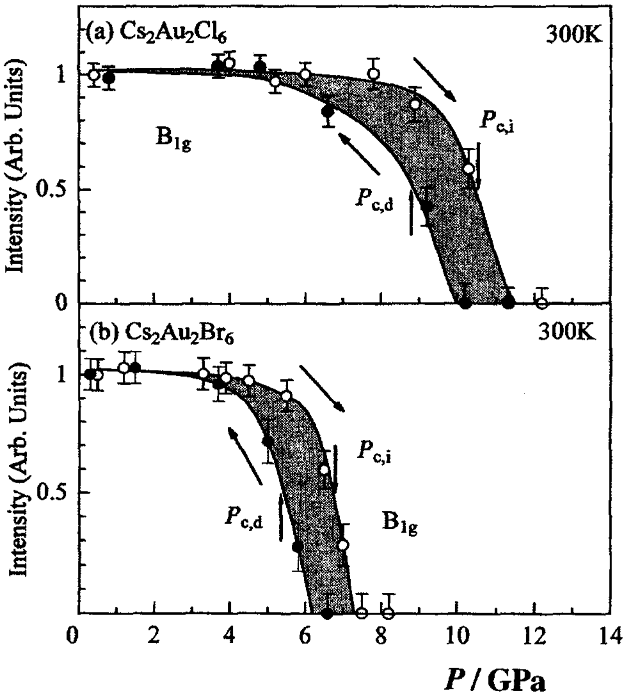

Fig. 18. Pressure dependence of intensities of the B_{1g} modes for (a) $Cs_2Au_2Cl_6$ and (b) $Cs_2Au_2Br_6$ at 300 K. Open and closed circles show the data obtained in the pressure-increasing and pressure-decreasing runs, respectively. $P_{c,i}$ and $P_{c,d}$ represent the critical pressures in the respective runs. Hatchings indicate pressure hysteresis (Ref. 75).

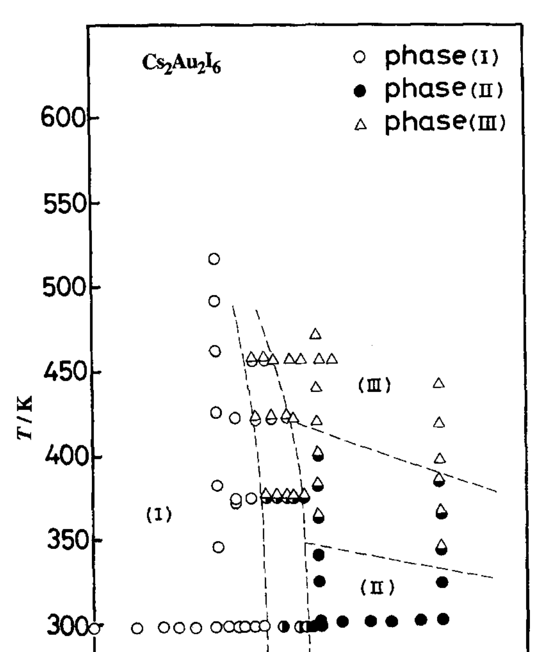

Fig. 19. P–T phase diagram of $Cs_2Au_2I_6$. (I): tetragonal (I) phase, (II): tetragonal (II) phase, (III): cubic phase (Ref. 64).

trical resistivity parallel and perpendicular to the c-axis of $Cs_2Au_2I_6$ at room temperature.[61] As the pressure is increased, the resistivity decreases by ten orders of magnitude down to the region of metal from ambient pressure. On the other hand, just above 5.0 GPa, both the resistivities of $\|c$ and $\perp c$ increase rapidly by four orders of magnitude, then they remain unchanged between 6 and 8 GPa. The drastic resistivity jump around 5 GPa is attributed to the first order phase (I)-phase (II) transition. The first order phase transition is regarded as a band Jahn–Teller transition caused by realization of the Au^{II} valence state, where the lowering of the lattice symmetry may open a gap at the Fermi energy. In order to microscopically elucidate the origin of resistivity jump at 5 GPa, the detailed single crystal X-ray analysis for the second phase of $Cs_2Au_2I_6$ is indispensable.

According to our resistivity measurements of $Cs_2Au_2I_6$ under high pressures,[56,57] $Cs_2Au_2I_6$ undergoes a pressure-induced semiconductor-to-metal transition at 4.5 GPa and room temperature. Moreover, as shown in Fig. 21, when the temperature is increased at 6.5 GPa, the resistivity decreases and a steep drop occurs at about 300 K and then it increases linearly above about 400 K. Comparing the behavior of the resistivity with the X-ray diffraction profiles in the vicinity of the tetragonal-to-cubic phase transition, the drastic resistivity drop at about 300 K and the linear increase in the resistivity above 400 K are attributed to the beginning and the end of the phase transition, respectively. In the cooling process, the resistivity decreases linearly with temperature cooled down to room temperature, which implies that the cubic phase can

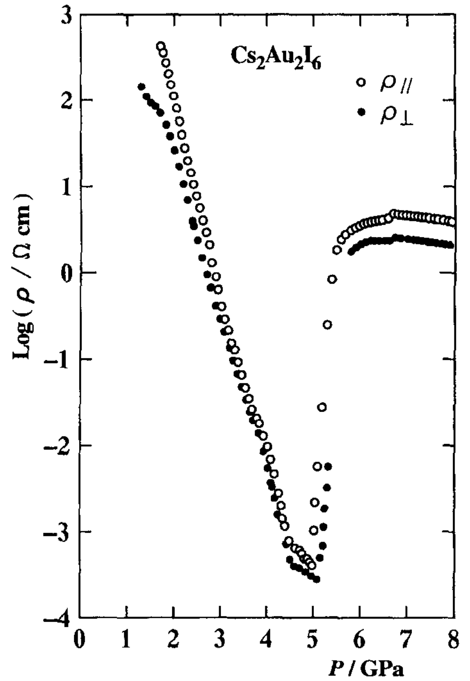

Fig. 20. Pressure dependence of the electrical resistivity of $Cs_2Au_2I_6$ at room temperature (Ref. 61).

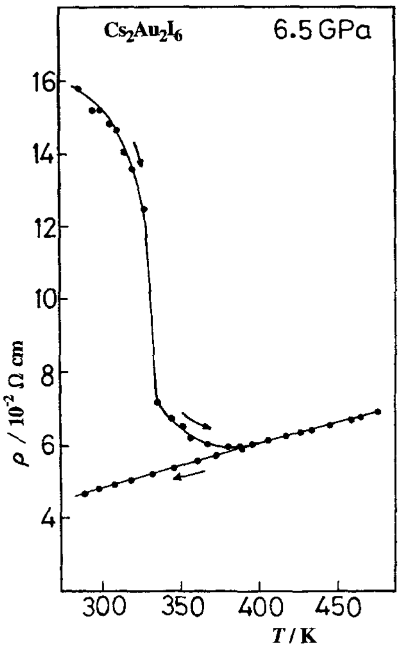

Fig. 21. Temperature dependence of the electrical resistivity of $Cs_2Au_2I_6$ at 6.5 GPa. The sample was first heated up to 470 K, then cooled down to room temperature (Ref. 56).

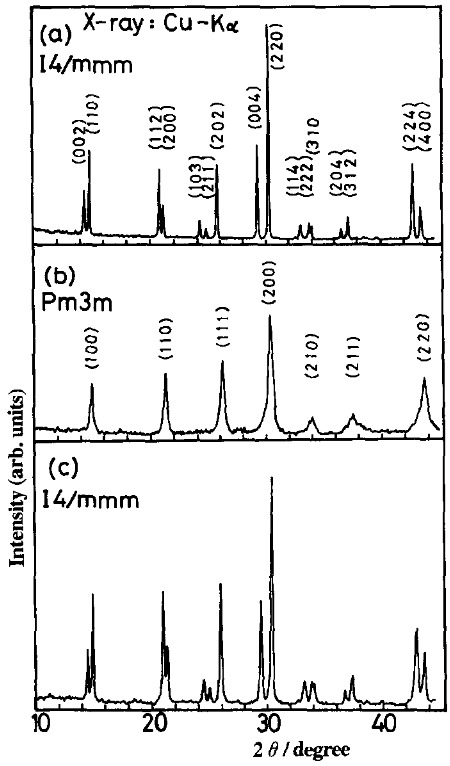

Fig. 22. X-ray powder patterns of $Cs_2Au_2I_6$ at room temperature and ambient pressure. (a) X-ray pattern before applying pressures. (b) X-ray pattern of the metastable phase obtained by decreasing temperature and pressure after increasing pressure up to 6.5 GPa and increasing temperature up to 480 K. (c) X-ray pattern after annealing the metastable phase at 370 K (Ref. 57).

be stable at 6.5 GPa and room temperature. Moreover, this metallic phase could be obtained as a metastable phase at ambient pressure and room temperature by decreasing the temperature and pressure after increasing pressure up to 6.5 GPa and temperature up to 470 K. Figure 22 shows the X-ray powder pattern of the metastable phase of $Cs_2Au_2I_6$, which implies that the metallic metastable phase is a cubic perovskite structure. After annealing at 373 K for 1 h, the metastable cubic phase converts into the stable tetragonal phase. In fact, as shown in Fig. 23, the metastable cubic phase shows a broad exothermic peak in the differential-scanning-analysis (DSC) curve around 355 K.

Figure 24 schematically shows the process to obtain the metastable cubic phase of $Cs_2Au_2I_6$. The metastable cubic phase can commonly be obtained for $Cs_2Au_2X_6$ (X = Cl, Br, and I) and $Rb_2Au_2I_6$.

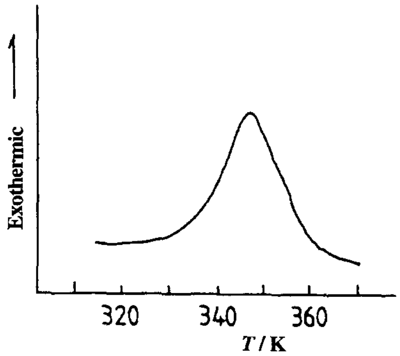

Fig. 23. Differential scanning analysis (DSC) curve for $Cs_2Au_2I_6$ after the release of pressure at room temperature (Ref. 58).

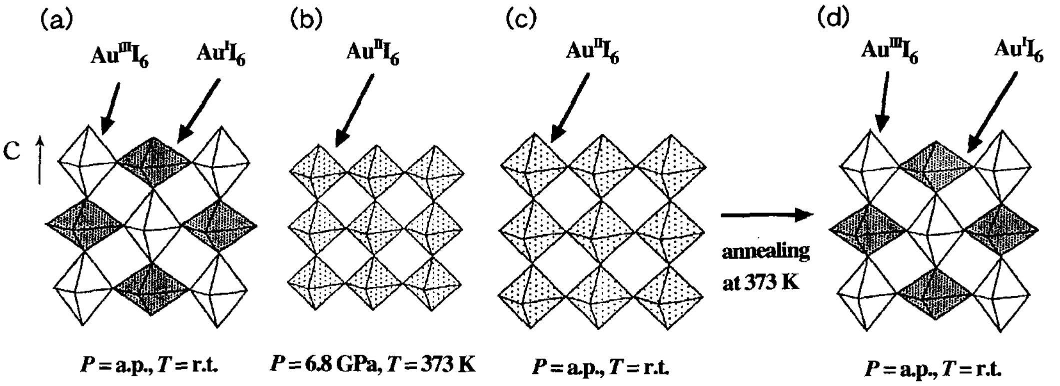

Fig. 24. Schematic process to obtain the metastable cubic phase of $Cs_2Au_2I_6$ at room temperature and ambient pressure.

7. Photo-Induced Gold Valence Transition

One of the recent topics of solid state physics is photo-induced transformation of electronic and magnetic state of materials. Several compounds, e.g., polydiacetylene[91] and cobalt-iron cyanide,[92] have been revealed to be photo-inducible, and such results are creating a new field of solid state science. In these compounds, however, the interrelation between the photo-excited state and the second phase is not so clear, which seems to be a barrier for true comprehension of the photo-induced effects. To overcome this disadvantage, we should explore a new photo-induced material whose phase transition as well as electronic structure is well understood.

As mentioned in the previous section, the pressure-induced structural phase transition of $Cs_2Au_2X_6$ is of first order and is coupled with the Au valence transition. Moreover, the cubic phase having Au^{II} state can be obtained as a metastable phase even at ambient pressure and room temperature. These phenomena imply the possibility of photo-induced phase transition by the light-irradiation corresponding to the Au^{I}–Au^{III} charge transfer band. Very recently, Liu, et al. have discovered a photo-induced Au valence transition for $Cs_2Au_2Br_6$ by means of Raman spectroscopy.[77]

Figure 25 shows the Raman scattering spectra in the bistable region at 300 K for $Cs_2Au_2Br_6$. Before photo-excitation (upper spectra of Fig. 25), the system is in the mixed-valence (MV) phase with the intense Au–Br stretching mode. The Raman signal completely disappears (middle spectra) after photo-excitation with 2000 pulse shots, due to the photo-induced phase transition into the single-valence (SV) phase. The excitation energy and photon density are 1.9 eV and 3.6×10^{16} cm^{-2} per pulse, respectively. Disappearance of the Raman signal is not due to deterioration of the sample surface. In fact, the photo-induced phase transition can be repeated several times with the same crystal. The bottom spectra of Fig. 25 show an example: The Raman signal nearly recovers after pressure-annealing procedure, that is, the pressure is released down to 3 GPa and then increased up to 6.1 GPa. The photo-induced phase transition of present system is one-way, i.e., only from the mixed-valence phase to the single valence phase. This is presumably due to the different electronic structures in each phase. In the mixed valence phase, as shown in Fig. 8, the spectral weight due to the IVCT is dominant in the visible region. The spectral weight, however, would transfer into the infrared region in the highly conductive single valence phase.

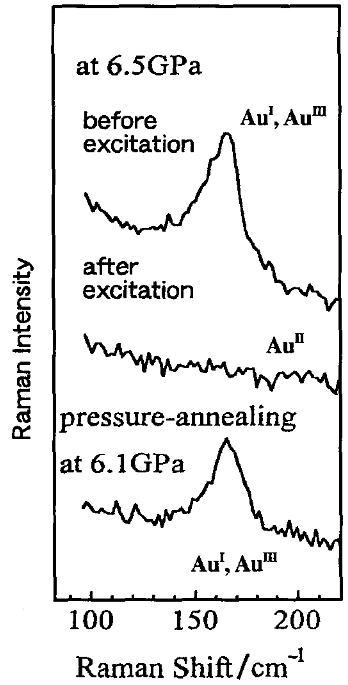

Fig. 25. Raman scattering spectra in the bistable region at 300 K for $Cs_2Au_2Br_6$ before (upper spectra) and after (middle spectra) photo-excitation: Initial state is the mixed valence (MV) phase. Excitation energy E_{exc} is 1.9 eV and pulse duration is 20 ns. Photon density per pulse is 3.6×10^{16} cm^{-2}. 2000 pulses shots are irradiated through the diamond window. the bottom spectrum was measured after pressure-annealing (Ref. 77).

The photo-induced phase transition of $Cs_2Au_2Br_6$ shows a threshold behavior against the excitation photon density and number of shots. In Fig. 26 are shown relative Raman intensity (I/I_0), where I_0 is the intensity before photo-excitation, against (a) photon density (shots number in fixed at 1000) and (b) number of shots (photon density is fixed at 2.4×10^{16} cm^{-2}). The I/I_0 represents the relative volume of $V_{MV}/(V_{MV}+V_{SV})$. In Fig. 26(a), the I/I_0 is nearly constant in the weak excitation condition, but suddenly drops down to

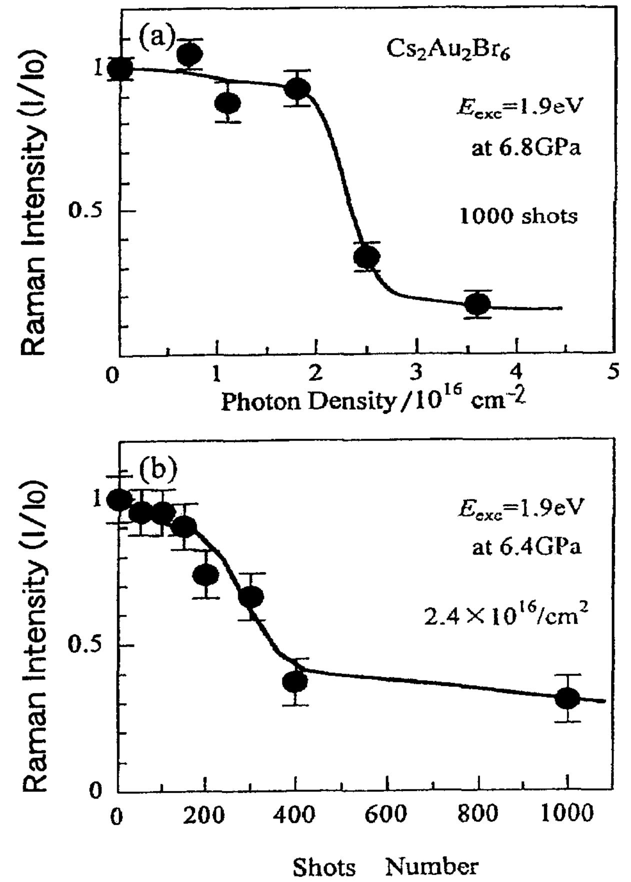

Fig. 26. (a) Photon density and (b) shots number dependence of relative Raman intensity I/I_0 of the Au–Br stretching mode in $Cs_2Au_2Br_6$, where I_0 is the intensity before photoexcitation. The Raman mode is deactivated in the photogenerated Au^{II} phase (Ref. 77).

about 0.2 when the photon density exceeds the critical value of 2×10^{16} cm^{-2}. Similar threshold behavior is also observed in the shot number dependence of the I/I_0: The intensity suddenly drops when the irradiation exceeds 300 shots, which is shown in Fig. 26(b). This phenomenon is explained as follows. In the $Au^{I,III}$ mixed valence phase of $Cs_2Au_2Br_6$, Au^I and Au^{III} states alternate three-dimensionally. The photoirradiation, however, transfers *d*-electrons from Au^I to Au^{III} sites and produces Au^{II} pairs. Such Au^{II} pairs would form a cluster state if the photon density were large enough. From a phenomenological point of view, the first-order phase transition is triggered when the clusters of the second phase (SV) grow to the critical value of $r_c = 2\sigma/\Delta E$, where σ and ΔE are the surface energy and the difference in the free energy between two phases.[93] With increase of photon density or of shot number, the size r of the photo-generated SV clusters reaches r_c. At the same time, the macroscopic MV–SV phase transition is triggered. The photo-induced Au valence transition in $Cs_2Au_2Br_6$ is schematically shown in Fig. 27.

9. Metallic Mixed Valence State

With the discovery of high Tc superconductors, research on polarons and bipolarons has gained renewed attention

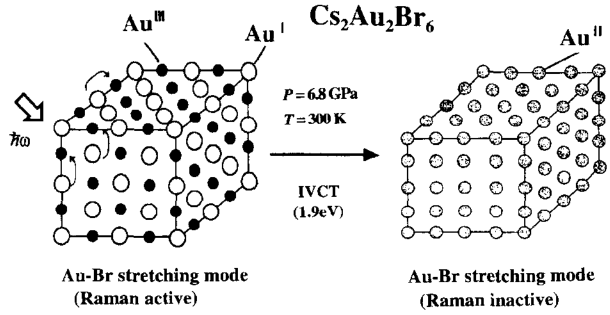

Fig. 27. Schematic photo-induced gold valence transition for $Cs_2Au_2Br_6$.

(e.g. see Refs. 1 and 2). According to the bipolaron model, $M_2Au^IAu^{III}X_6$ is regarded as an on-site bipolaron system (i.e. negative U system), where the bipolarons form a three-dimensional lattice and localize at the Au^I site. In this section, from the viewpoint of the bipolaron model, we focus on the metallic mixed valence state in $Cs_2Au_2Cl_6$.

Recently, Kojima et al. have measured the single crystal resistivity of $Cs_2Au_2Cl_6$ under high pressures and low temperatures by using a standard four-probe method.[70] Figure 28 shows the temperature dependence of the electrical resistivity of $Cs_2Au_2Cl_6$under the pressure region below the Au valence transition (11—12 GPa).[70] At 5.0 GPa, a gradual semiconductor-to-metal transition occurs about 250 K. With decreasing temperature, the resistivity decreases slowly from 250 to 100 K and then it increases below 100 K. At 6.0 GPa, the metallic region becomes to be spread between 250 and 5 K. Under the pressure region above 7.0 GPa, the resistivity as a function of temperature is metallic over the whole temperature region of measurements.

According to the ^{197}Au Mössbauer spectra of $Cs_2Au_2Cl_6$,[47,48] which is shown in Fig. 29,[47] the Au^I and

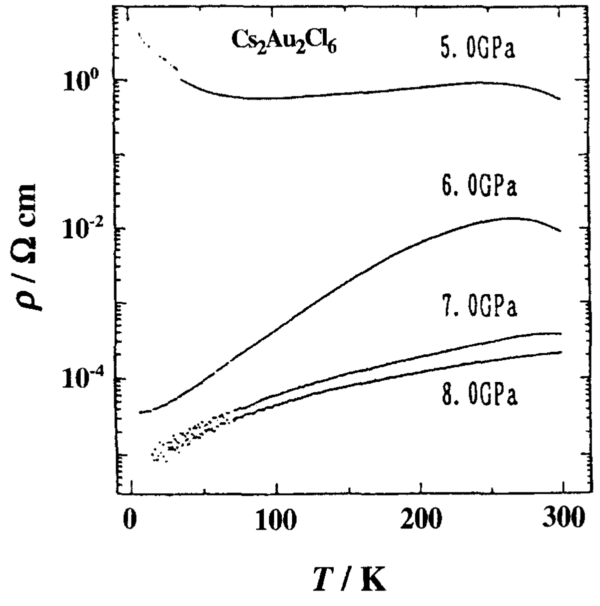

Fig. 28. Temperature dependence of the electrical resistivity perpendicular to the *c*-axis of $Cs_2Au_2Cl_6$ at various pressures (Ref. 70).

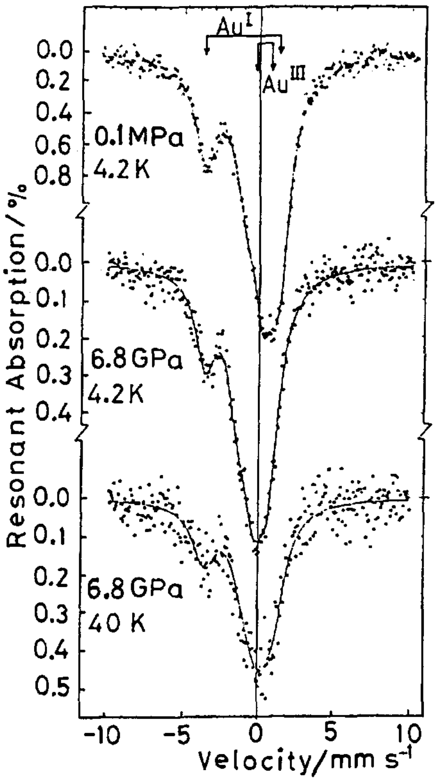

Fig. 29. ^{197}Au Mössbauer spectra of $Cs_2Au_2Cl_6$ at ambient pressure and 6.8 GPa (Ref. 47).

Au^{III} states are clearly distinguishable even at 6.8 GPa and the Au^{II} state can hardly be detected in the time scale of ^{197}Au Mössbauer spectroscopy ($\tau = 1.91 \times 10^{-9}$ s). If one includes the ^{197}Au Mössbauer spectra and the transport phenomena of $Cs_2Au_2Cl_6$ under high pressures, the Au valence states of $Cs_2Au_2Cl_6$ at 4.2 K and ambient pressure and at 4.2 K and $P = 6.8$ GPa can be schematically shown as in Figs. 30(a) and 30(b), respectively. At ambient pressure, the filled Au^{I} site and the empty Au^{III} site of $Cs_2Au_2Cl_6$ are deeply localized. Thus the bipolaron lattice of Au^{I} and Au^{III} shown in Fig. 30(a) is rigid, which reflects the completely insulating character of $Cs_2Au_2Cl_6$ at ambient pressure. On the other hand, with increasing pressure, the difference in the octahedral size between Au^{I}Cl$_6$ and Au^{III}Cl$_6$ in $Cs_2Au_2Cl_6$ becomes small, in other words, the electron-phonon interaction decreases. Moreover, the charge transfer interaction between Au^{I} and Au^{III} increases with pressure. Under high pressure, owing to the overlap of the wave functions of the Au^{I} and Au^{III} sites, the bipolarons can tunnel between adjacent Au sites at low temperature, eventually the rigid bipolaron lattice presumably begin to melt and highly mobile bipolarons appear, which is schematically shown in Fig. 30(b). As shown in Fig. 29, the spectral profile at 4.2 K and 6.8 GPa closely resembles that at 4.2 K and 0.0 Gpa (ambient pressure), which strongly implies that the metallic behavior in the phase I of $Cs_2Au_2Cl_6$ can be attributed to the dynamic two-electron exchange between Au^{I} and Au^{III} sites (i.e. highly mobile bipolaron).

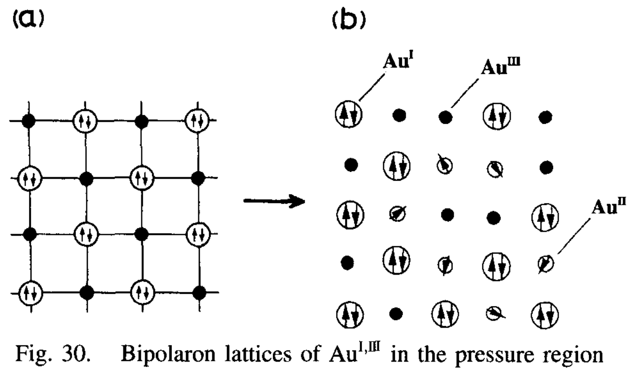

Fig. 30. Bipolaron lattices of Au^{I,III} in the pressure region below the Au valence transition.

Recently, Liu et al. have discovered an anomalously broad Raman band due to the Au–X stretching mode in the metallic mixed-valence phase for $Cs_2Au_2X_6$ (X = Cl and Br).[76] As mentioned in Sect. 5.3, the Au–X stretching mode is Raman active only in the mixed-valence state. Therefore, the anomalously broad Au–X stretching mode would support the melting of the Au^{I,III} bipolaron lattice. In connection with the melting of bipolaron lattice, in order to prove the existence of highly mobile bipolarons, the measurement of carrier-density in the metallic mixed-valence phase of $Cs_2Au_2X_6$ is indispensable and is in progress.

According to recent bipolaron theory,[52—55] an unusual superconductor due to the Bose condensation of bipolarons is expected under some electron–phonon coupling constant, λ, while in the large limit of λ, a bipolaron insulator occurs. In the case of gold mixed-valence system, from the resistivity measurements up to 8 GPa and down to 5 K, a superconducting phase has not yet been observed. Recently, Varma proposed a theoretical model with negative U effect, which gives a superconducting phase in the carrier density region far from the half-filling in agreement with the properties of $BaPb_{1-x}Bi_xO_3$ and $Ba_{1-x}K_xBiO_3$.[94] From this model, the substitution of Cs or Au with Ba or Hg might be indispensable for researches on the superconducting phase.

This work has been created in collaboration with Dr. H. Kitagawa (JAIST), Prof. O. Shimomura (Japan Atomic Energy Research Institute), Dr. T. Kikegawa (High Energy Accelerator Research Organization), Prof. N. Môri (ISSP, Univ. Tokyo), Prof. H. Takahashi (Nihon Univ.), Profs. M. Seto and Yu. Maeda (KUR, Kyoto Univ.), Dr. X.J. Liu and Profs. Y. Moritomo and A. Nakamura (Nagoya Univ.), Dr. J. Stanek (Jagiellonian Univ.), Prof. S.S. Hafner and Drs. Li. Zhang and H. Ahsbahs (Marburg Univ.), Prof. N. Matsushita and Mr. S. Matsuba (Univ. Tokyo), and Mr. F. Amita (Kyoto Univ.). The author wish to thank for these collaborators. This work has partly been supported by a Grant-in-Aid for Science Research from the Ministry of Education, Science, Sports and Culture.

References

1 "Mixed Valency Systems: Applications in Chemistry, Physics and Biology," ed by K. Prassides, Kluwer Academic Publishers, (1991).

2 "Polarons and Bipolarons in High-T_c Superconductors and Related Materials," ed by. E. K. H. Salje, A. S. Alexandrov, and W. Y. Liang, Cambridge University Press, (1995).

3 P. Day, in "Low-Dimensional Cooperative Phenomena," ed by H. J. Keller, Plenum Press, New York (1974), p. 191.

4 R. J. H. Clark, M. L. Franks, and W. R. Trumble, *Chem. Phys. Lett.*, **41**, 287 (1976).

5 H. J. Keller, in "Extended Linear Chain Compounds," ed by J. S. Miller, Plenum Press, New York (1982), Vol. 1, p. 357.

6 D. S. Martin, Jr., in "Extended Linear Chain Compounds," ed by J. S. Miller, Plenum Press, New York (1982), Vol. 1, p. 409

7 R. J. H. Clark, *Chem. Soc. Rev.*, **13**, 219 (1984); **19**, 107 (1990).

8 H. Tanino and K. Kobayashi, *J. Phys. Soc. Jpn.*, **52**, 1446 (1983).

9 K. Nasu, *J. Phys. Soc. Jpn.*, **52**, 3865 (1983); **53**, 427 (1984); **54**, 1933 (1985).

10 M. Tanaka, S. Kurita, Y. Okada, T. Kojima, and Y. Yamada, *Chem. Phys.*, **91**, 257 (1984).

11 Y. Wada, T. Mitani, M. Yamashita, and T. Koda, *J. Phys. Soc. Jpn.*, **54**, 3143 (1985).

12 P. Day, in "Organic and Inorganic Low-Dimensional Crystalline Materials," ed by P. Delhaes and M. Drillon, Plenum Press, New York (1987).

13 A. Kawamori, R. Aoki, and M. Yamashita, *J. Phys. C: Solid State Phys.*, **18**, 5487 (1985).

14 M. Tanaka and I. Tsujikawa, *Acta Crystallogr., Sect. C*, **C42**, 1105 (1986).

15 N. Kuroda, M. Sakai, Y. Nishina, M. Tanaka, and S. Kurita, *Phys. Rev. Lett.*, **58**, 2212 (1987).

16 N. Matsushita, N. Kojima, T. Ban, and I. Tsujikawa, *J. Phys. Soc. Jpn.*, **56**, 3808 (1987).

17 S. Kurita, M. Haruki, and K. Miyagawa, *J. Phys. Soc. Jpn.*, **57**, 1789 (1988).

18 M. Haruki and S. Kurita, *Phys. Rev.*, **B39**, 5706 (1989).

19 Y. Wada, K. Era, and M. Yamashita, *Solid State Commun.*, **67**, 953 (1988).

20 D. Baeriswyl and A. R. Bishop, *J. Phys. C: Solid State Phys.*, **21**, 339 (1988).

21 N. Matsushita, N. Kojima, N. Watanabe, and T. Ban, *Solid State Commun.*, **71**, 253 (1989).

22 R. J. Donohoe, S. A. Ekberg, C. D. Tait, and B. I. Swanson, *Solid State Commun.*, **71**, 49 (1989).

23 N. Kuroda, M. Sakai, M. Suezawa, Y. Nishina, and K. Sumino, *J. Phys. Soc. Jpn.*, **59**, 3049 (1990).

24 H. Okamoto, K. Toriumi, T. Mitani, and M. Yamashita, *Phys. Rev.*, **B42**, 10381 (1990).

25 R. Ikeda, M. Iida, T. Asaji, and A. Ghosh, *Chem. Phys. Lett.*, **210**, 229 (1993).

26 H. Ooi, M. Yamashita, and T. Kobayashi, *Solid State Commun.*, **86**, 789 (1993).

27 Y. Wada, U. Lemmer, E. O. Göbel, M. Yamashita, and K. Toriumi, *Phys. Rev.*, **B52**, 8276 (1995).

28 A. Mishima and K. Nasu, *Phys. Rev.*, **B39**, 5758 and 5763 (1989).

29 Y. Tagawa and N. Suzuki, *J. Phys. Soc. Jpn.*, **59**, 4074 (1990); **64**, 1800 (1995); **64**, 2212 (1995).

30 J. T. Gammel, A. Saxena, I. Batistic, A. R. Bishop, and S. R. Phillpot, *Phys. Rev.*, **B45**, 6408 (1992).

31 H. Okamoto and, M. Yamashita, *Bull. Chem. Soc. Jpn.*, **71**, 2023 (1998).

32 "Relaxations of Excited States and Photo-Induced Structural Phase Transitions," ed by K. Nasu, Springer, (1997).

33 H. L. Wells, *Am. J. Sci.*, **3**, 315 (1922).

34 N. Elliott, *J. Chem. Phys.*, **2**, 419 (1934).

35 N. Elliott and L. Pauling, *J. Am. Chem. Soc.*, **60**, 1846 (1938).

36 G. Brauer and G. Sleater, *J. Less-Common Metals*, **21**, 283 (1970)

37 J. Strähle, J. Gelinek, M. Kölmel, and A. Nemecek, *Z. Naturforsch., B*, **34b**, 1047 (1979).

38 J. Bill, K. Lerch, and W. Laqua, *Z. Anorg. Allg. Chem.*, **589**, 7 (1990).

39 J. Strähle, J. Gelinek, and M. Kölmel, *Z. Anorg. Allg. Chem.*, **456**, 241 (1979).

40 H. Kitagawa, N. Kojima, N. Matsushita, T. Ban, and I. Tsujikawa, *J. Chem. Soc., Dalton Trans.*, **1991**, 3115.

41 P. Gütlich, B. Lehnis, K. Römhild, and J. Strähle, *Z. Naturforsch., B*, **37b**, 550 (1982).

42 J. C. M. Tindemans-v. Eijndhoven and G. C. Verschoor, *Mat. Res. Bull.*, **9**, 1667 (1974).

43 R. Keller, J. Fenner, and W. B. Holzapfel, *Mat. Res. Bull.*, **9**, 1363 (1974).

44 W. Denner, H. Schulz, and H. D'Amour, *Acta Crystallogr., Sect. A*, **A35**, 360 (1979).

45 P. Day, C. Vettier, and G. Parisot, *Inorg. Chem.*, **17**, 2319 (1978).

46 M. Katada, Y. Uchida, K. Sato, H. Sano, H. Sakai, and Yu. Maeda, *Bull. Chem. Soc. Jpn.*, **55**, 444 (1982).

47 J. Stanek, S. S. Hafner, and H. Schulz, *Phys. Lett.*, **A76**, 333 (1980).

48 J. Stanek, *J. Chem. Phys.*, **76**, 2315 (1982).

49 H. Tanino and K. Takahashi, *Solid State Commun.*, **59**, 825 (1986).

50 J. G. Bednorz and K. A. Müller, *Z. Phys.*, **B64**, 189 (1986).

51 R. J. Cava, B. Batlogg, J. J. Krajewski, R. Farrow, L. W. Rupp, Jr., A. E. White, K. Short, W. F. Peck, and K. Kometani, *Nature*, **332**, 81 (1988).

52 B. K. Chakraverty, *J. Phys. Lett.*, **40**, L99 (1979).

53 A. S. Alexandrov and J. Ranninger, *Phys. Rev.*, **B23**, 1796 (1981).

54 A. S. Alexandrov, J. Ranninger, and S. Robaszkiewicz, *Phys. Rev.*, **B33**, 4526 (1986).

55 D. Emin and M. S. Hillery, *Phys. Rev.*, **B39**, 6575 (1989).

56 N. Kojima, H. Kitagawa, T. Ban, F. Amita, and M. Nakahara, *Solid State Commun.*, **73**, 743 (1990).

57 N. Kojima, H. Kitagawa, T. Ban, F. Amita, and M. Nakahara, *Synth. Met.*, **41-43**, 2347 (1991).

58 H. Kitagawa, H. Sato, N. Kojima, T. Kikegawa, and O. Shimomura, *Synth. Met.*, **41-43**, 1953 (1991); *Solid State Commun.*, **78**, 989 (1991).

59 H. Kitagawa, N. Kojima, and T. Nakajima, *J. Chem. Soc., Dalton Trans.*, **1991**, 3121.

60 H. Kitagawa, N. Kojima, and H. Sakai, *J. Chem. Soc., Dalton Trans.*, **1991**, 3211.

61 H. Kitagawa, N. Kojima, H. Takahashi, and N. Môri, *Synth. Met.*, **55-57**, 1726 (1993).

62 N. Kojima, F. Amita, H. Kitagawa, H. Sakai, and Yu. Maeda, *Nucl. Instr. Method. Phys. Res.*, **B76**, 321 (1993).

63 N. Kojima, A. Tanaka, H. Sakai, and Yu. Maeda, *Nucl. Instr. Method. Phys. Res.*, **B76**, 366 (1993).

64 N. Kojima, M. Hasegawa, H. Kitagawa, T. Kikegawa, and O. Shimomura, *J. Am. Chem. Soc.*, **116**, 11368 (1994).

65 N. Kojima and H. Kitagawa, *J. Chem. Soc., Dalton Trans.*, **1994**, 327.

66 S. S. Hafner, N. Kojima, J. Stanek, and Li. Zhang, *Phys. Lett.*, **A192**, 385 (1994).

67 N. Kojima, M. Seto, and Yu. Maeda, *Soc. Ital. Fis.*, **50**, 43 (1996).

68 N. Kojima, H. Sakai, M. Seto, S. Kitao, and Yu. Maeda, *Soc. Ital. Fis.*, **50**, 47 (1996).

69 N. Kojima, *Mol. Cryst. Liq. Cryst.*, **285**, 295 (1996).

70 N. Kojima, F. Fukuhara, H. Kitagawa, H. Takahashi, and N. Môri, *Synth. Met.*, **86**, 2175 (1997).

71 N. Matsushita, H. Kitagawa, and N. Kojima, *Acta Crystallogr., Sect. C*, **C53**, 663 (1997).

72 A. Ishikawa, M. Kurasawa, S. Kitahara, A. Sasane, N. Kojima, and R. Ikeda, *Z. Naturforsch., A*, **53a**, 590 (1998).

73 N. Matsushita, H. Ahsbahs, S. S. Hafner, and N. Kojima, *Rev. High Pressure Sci. Technol.*, **7**, 329 (1998).

74 X. J. Liu, K. Matsushita, Y. Moritomo, A. Nakamura, and N. Kojima, *Phys. Rev.*, **B59**, 7925 (1999).

75 X. J. Liu, Y. Moritomo, A. Nakamura, and N. Kojima, *J. Chem. Phys.*, **110**, 9174 (1999).

76 X. J. Liu, Y. Moritomo, A. Nakamura, and N. Kojima, *J. Phys. Soc. Jpn.*, **68**, 3134 (1999).

77 X. J. Liu, Y. Moritomo, M. Ichida, A. Nakamura, and N. Kojima, *Phys. Rev.*, **B61**, 20 (2000).

78 P. Pyykkö and J. P. Desclaux, *Acc. Chem. Res.*, **12**, 276 (1979).

79 D. Guenzburger and D. E. Ellis, *Phys. Rev.*, **B22**, 4203 (1980).

80 P. Braunstein, U. Schubert, and M. Burgard, *Inorg. Chem.*, **23**, 4057 (1984).

81 P. G. Jones, A. G. Maddock, M. J. Mays, M. M. Muir, and A. F. Williams, *J. Chem. Soc., Dalton Trans.*, **1977**, 1434.

82 R. V. Parish, *Gold. Bull.*, **15**, 51 (1982).

83 H. Prosser, F. E. Wagner, G. Wortmann, G. M. Kalvius, and R. Wäppling, *Hyperfine Interact.*, **1**, 25 (1975).

84 M. B. Robin and P. Day, *Adv. Inorg. Chem. Radiochem.*, **10**, 247 (1967).

85 H. Kitagawa, H. Okamoto, and T. Mitani, private communication.

86 L. E. Orgel, *J. Chem. Soc.*, **1958**, 4186.

87 M. H. L. Pryce, K. P. Sinha, and Y. Tanabe, *Mol. Phys.*, **9**, 33 (1965).

88 G. Wingefeld and R. Hoppe, *Z. Anorg. Allg. Chem.*, **516**, 223 (1984).

89 H. Effenberger, *Z. Kristallogr.*, **188**, 43 (1989).

90 B. G. Müller, *J. Fluorine Chem.*, **17**, 317 (1981).

91 S. Koshihara, Y. Tokura, K. Kakeda, and T. Koda, *Phys. Rev. Lett.*, **68**, 1148 (1992).

92 O. Sato, T. Iyoda, A. Fujishima, and K. Hashimoto, *Science*, **272**, 704 (1996).

93 J. S. Langer, *Ann. Phys.*, **41**, 108 (1967).

94 C. M. Varma, *Phys. Rev. Lett.*, **61**, 2713 (1988).

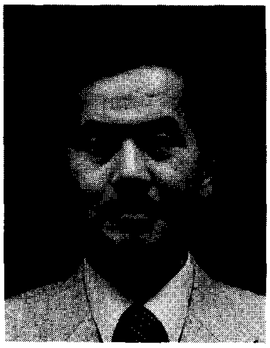

Norimichi Kojima was born in 1949 in Tottori city, Japan. He received his B. Sc. degree in 1972, M. Sc. in 1974, and D. Sci. in 1978 from Kyoto University. After the graduation, he joined the Broadcasting Science Research Laboratories of Japan Broadcasting Corporation (NHK). In 1981, he was appointed as lecturer in Kobe Tokiwa College. In 1984, he was appointed as research associate in Kyoto University and promoted as associate professor in the same university. In 1994, he was promoted as full professor in the University of Tokyo. His current interests include the solid state science, especially optical, magnetic, and transport properties of transition metal complexes.